Electronic Thesis and Dissertation Repository

12-12-2019 3:30 PM

The effects of turbulent cross-winds on combusting jets at low velocity ratios

Md Mahbub Hossain, *The University of Western Ontario*

Supervisor: Kopp, Gregory A., *The University of Western Ontario*
A thesis submitted in partial fulfillment of the requirements for the Master of Engineering
Science degree in Mechanical and Materials Engineering
© Md Mahbub Hossain 2019

Follow this and additional works at: https://ir.lib.uwo.ca/etd

Abstract

Gas flares have been distinguished as a potential major source of hydrocarbon emissions from refineries and chemical plants. Flaring is the burning of waste gasses through a flare stack or other combustion device. By generating atmospheric turbulence in wind tunnel, an in-depth study has been conducted to capture the mechanics involving the reactive jet and stack-wake regions, which resembles the real world scenario of gas flaring, but at a reduced scale. In this study, a methodology has been described to generate atmospheric turbulence by passive grid to obtain the ideal turbulence intensities (I_u) and length scales (L_x) for model flare stacks.

The entire flame is depicted by capturing flame images using multiple cameras. How the upstream turbulent flow interacts with non-premixed reactive jets at low velocity ratios is examined. The size of the recirculation zone decreases with an enhanced turbulent cross-wind. In addition to that, a comprehensive study of discrete flame packets are carried out using instantaneous images. The colour of the flame is closely analyzed in order to distinguish the mixing phenomena of crossflow fluid and jet fluid in the near field. Moreover, an empirical equation is proposed for predicting flame length in the presence of cross-wind. The changes in flame length, discrete flame packets, and colour are monitored for the different upstream turbulent cross-winds. It is observed in the current study that cross-wind turbulence affects the flame lengths, wake recirculation zone, vertical and lateral spread of the flame.

Keywords: Atmospheric turbulence; flame length; flame spread; discrete flame packets

Summary for Lay Audience

Gas flaring from industrial establishments and production sites are a common real world phenomenon. In 2012, researchers report tracking flares using an instrument aboard a NASA weather satellite that takes images of Earth in infrared and visible light which indicated that the total flared gas volume was approximately 143 billion cubic meters (BCM), corresponding to 3.5% of global production. Flared gas contributes significantly to global warming since the burned product CO_2 is directly responsible for enhancing greenhouse effects. Johnson and Kostiuk(2002) reported that some of the flared gas remain unburned due to the presence of strong cross-wind. The unburned fuel (specifically methane) is twenty times more harmful in causing greenhouse effects.

In the current study, atmospheric turbulence is generated in reduced scale in the wind tunnel. Gas flaring phenomena is observed for different turbulence conditions. Multiple cameras are used for flame visualization. An empirical equation is provided to predict flame length for methane rich fuel. The changes in flame length, discrete flame packets, dispersion or spread of visible flame, and the colour of flames are monitored for the different upstream turbulent conditions. The current study shows that crossflow turbulence affects the above mentioned properties. The current study suggests that tracking unburned fuel will assist to identify turbulence effects on flaring phenomena more clearly.

Acknowledgments

I wish to offer my sincere thanks to Professor Gregory Kopp, a great supervisor, mentor. Dr. Kopp has supported me above and beyond what I could ever expect. His guidance, patience, and encouragement throughout my graduate studies have taught me lessons on the workings of academic research. He has always been available for constructive discussions on my research. I have enjoyed my time working with him and look forward to continuing to work with him in the future.

I would also like to express my gratitude to Professor Larry Kostiuk and Professor Matthew Johnson. They have helped the progression of the experiments by providing ideas and constructive suggestions. I acknowledge the support of Mr. Darcy Corbin, who designed and built the experimental setup and helped me to familiarize with the experimental equipment. I would like to acknowledge the other research group members, particularly Dr. Chieh-Hsun Wu who was always open for technical discussions related to research. I would like to thank Mr. Mahtab Ahmed and Mr. Zaied Zaman for image processing discussions. I am also grateful to Ms. Diya Cui for her help during the experiment. I would also like to thank the Boundary Layer Wind Tunnel Laboratory staff and technicians for their help with the experimental portions of this research.

Finally, I would like to thank my friends for their support during this degree. I express my affectionate appreciation to my family, specially my mother. From my childhood till now, she has been sacrificing her happiness to make me happy.

Table of Contents

List of Tables

List of Figures

Nomenclature

b – Bar width of the grid

C_D – Co-efficient of drag

C_f – Concentration of fuel on jet

d – Inner diameter of stack

$E(\kappa)$ – Turbulent kinetic energy as a function of wave number

f – Eddy frequency

I_u – Turbulence intensity

J – Momentum ratio

κ - Wave number

K_f - flame constant

K_u – constant of proportionality

L_x – Integral length scale

L_F – Flame length

M – Mesh size of grid

P_∞ - Free stream pressure

P_{wake} – Pressure in wake region

r - velocity ratio

R_{uu} – Auto co-relation function

s- Density ratio

$S_{uu}(f)$ – Turbulent kinetic energy distribution in the frequency domain

U_∞/u_{mean}/ $\bar{u}$ – Mean streamwise/crossflow velocity

U_j – Mean jet velocity

X – Streamwise or crossflow direction

x – Distance from grid to experimental section

Y – Vertical direction

Z – Lateral direction

ΔY – Spread of flame in vertical direction

ΔZ – Spread of flame in lateral direction

Chapter 1

1   Introduction

1.1   Background

The jet injected in a cross stream is a classical three-dimensional flow which is significant in a wide range of engineering practice. The jet in crossflow (JICF) or transverse jet is utilized in dilution or primary air jet injection in gas turbine combustors, to accomplish mixture ratio and NO_x control as well as turbine hot section cooling; in film cooling of turbine blades; in primary fuel injection in high speed air breathing engines; and in thrust vector control for missiles and other high speed vehicles (Karagozian, 2014). In addition to mechanical engines, JICF studies are important for environmental cases, such as the effluent from a chimney into the environment and dispersion of particles. In the above-mentioned applications, a gaseous jet is injected into relatively quiescent surroundings or large scale cross flows.

Flaring of gas from industrial establishments in low jet to cross flow velocity ratios (r) is a continual real world happening (fig. 1.1). In 2012, researchers reported tracking flares using satellite images of Earth in the infrared and visible light range. These images indicated that the total flared gas volume was approximately 143 (13.6) billion cubic meters (BCM), corresponding to 3.5% of global production (Nature, 2016). Ninety percent of the flared gas volume was found in upstream production areas, 8% at downstream refineries and 2% at liquefied natural gas (LNG) terminals (Christopher et al., 2016). Those flared gases contribute to global warming as the burned product, CO_2, a greenhouse gas.

In most of the research cases, the jet in cross flow has been investigated for a round axisymmetric jet with mean velocity, U_j, injected perpendicularly into a steady crossflow with velocity, U_∞ ((Keffer and Baines, 1963), (Fric and Roshko, 1994), (Kelso et al. ,1996)). Flow separation at leading edge, inclination of jet due to interaction with cross

stream, evolution of vorticity in the jet shear layer due to velocity-difference or density difference ((Z M Moussa, 1977), (J Andreopoulos, 1985), (Karagozian, 2010)) as well as pressure difference between the upstream and downstream region of circular jet stack (K Mahesh(2013)) are important characteristics that control the near field of the JICF.

The Jet Flame in Cross Flow (JFICF) exhibits a similar phenoma as the cold jet in crossflow. In this case, the heat released by combustion influences the flow field. Most of the experimental research on JFICF has been conducted at high velocity ratios. However, Brzustowski(1976), Huang and Chang(1994b), Kostiuk et al.(2000) focused on the study of flames at low velocity ratios. Smooth crossflows (i.e., low turbulence) is considered during experiments conducted in wind tunnels.

Figure 1.1: Large amount of gas is burned by gas flares [Shutterstock].

1.2   Jet in Cross Flow

Inherently, the jet in cross flow involves the perpendicular injection of jet fluid with a characteristic velocity, U_j, into a cross-flow, which has a velocity, U_∞. The jet is injected through a uniform cross-sectional nozzle elevated above from the floor or flush to a wall (fig. 1.2). As the jet fluid trajectory bends into the cross-flow direction, the characteristics of the interaction in terms of vorticity dynamics, shear layer stability, jet fluid penetration, and scaler mixing are highly dependent upon several flow parameters (Getsinger, 2012). The dominating flow parameters are velocity ratio (r), density ratio (s) and momentum flux ratio (J) defined as:

$$r = \frac{U_j}{U_\infty} \qquad\qquad 1.1$$

$$s = \frac{\rho_j}{\rho_\infty} \qquad\qquad 1.2$$

$$J = \frac{\rho_j\, U_j^2}{\rho_\infty\, U_\infty^2} \qquad\qquad 1.3$$
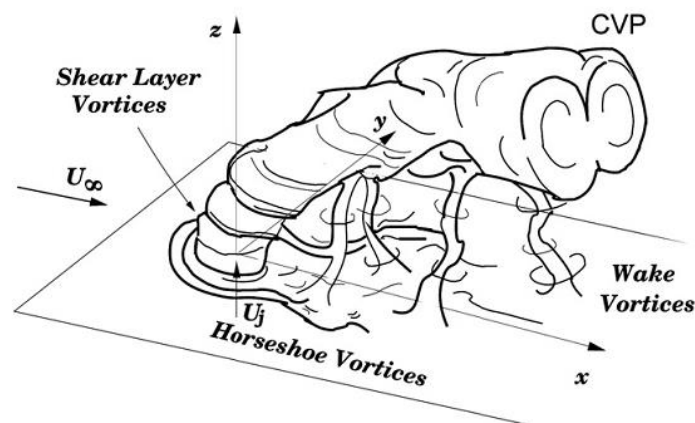
Figure 1.2: Schematic of traverse jet and relevent vortical structures (Modified from Fric and Roshko(1994)).

1.2.1 Cross-flow shear layer characteristics

Cross-flow shear layer instabilities are broadly assumed as a reason for the Kelvin-Helmholtz(KH) instability (Kelso et al., 1996 ; Fric and Roshko, 1994). KH instability appears because of velocity difference or density difference of two fluids as they interact with each other. Experimental observations $(2 < r < 10)$ by Fric & Roshko (1994) distinguished four distinct structures in the floor flushed transverse jet: the jet shear-layer vortices, the system of horseshoe vortices, counter-rotating vortex pair, and the wake vortices. In contrast, experiments with a thin slit in cross-flow (Blanchard et al., 1999) assert that the nearfield instabilities of JICF is not a result of the Kelvin-Helmholtz instability. In addition to that, Camussi et al.(2002), after conducting a water tunnel experiment at low velocity ratio $(1.5 < r < 4.5)$, also suggest that shear layer instabilities of JICF are different than the Kelvin-Helmholtz instability and more likely a result of waving or flapping of the jet flow. Both Camussi et al.(2002) and Blanchard et al. (1999) conducted their study at a low Reynolds numbers. This might be reason that the results of Kelso et al.(1996) and Fric and Roshko(1994) is more widely accepted.

Figure 1.3 represents the evolution of a vortex loop for the cold jet at low velocity ratio. The water tunnel flow visualization study of Lim et al.(2001) shed some light on the 'lateral roller' vortices on both the windward and leeward sides of the jet. In detail, Yuan et al.(1999) identified some near field structures which are the result of the Kelvin-Helmholtz instability and lead to 'lateral roller' that extend upward and downstream. Perturbations from the lateral rollers cause 'vertical streaks' or 'packet' type structures that are convected downstream. Lim et al.(2001) term these as loop type structures (fig. 1.3(a,b)) and add that at low velocity ratios(typically $1 < r$), those loop structure have been found to form only on the windward side (fig. 1.3c) of the jet. The orientation of their vortex loops suggests that 'jet structures' have transformed into 'wake structures'. Moreover, this model suggests that the large-scale structures of JICF consist essentially of loop vortices, that are not caused by the folding of the vortex rings which is unlike the observation given by Kelso et al.(1996). At low velocity ratio $(r < 1)$, the regular structures are broken up by the action

of the upstream shear layer and evolve as chaotic flow structures (Huang and Chang (1994)).
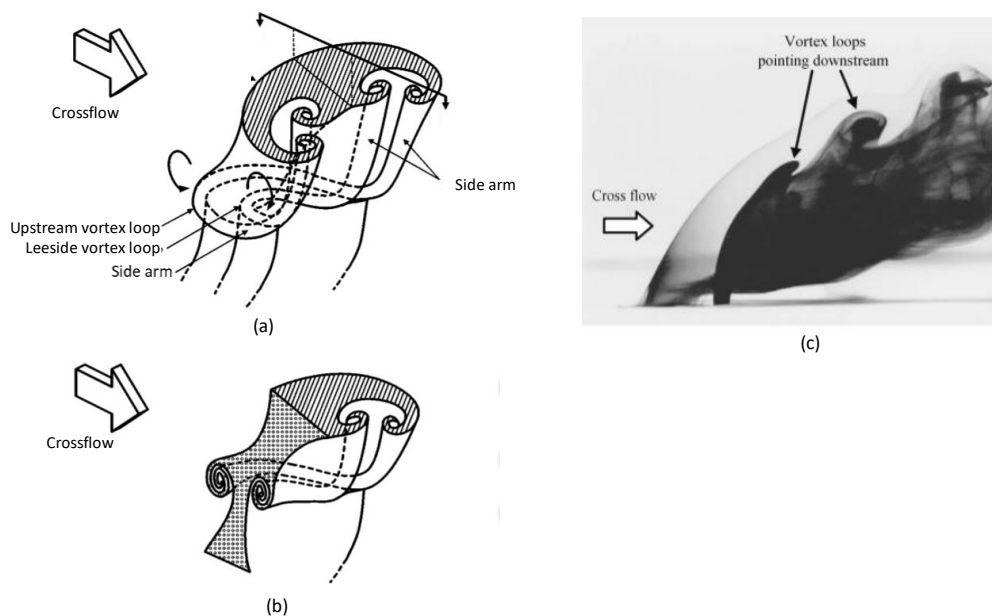
Figure 1.3: Details sketch of Lim et al.(2001) model. a) Evolution of vortex loops, b) section of the depicted jet, c) Wake structure of the nozzle at velocity ratio 1 (T H New (1998)).

1.3   Reacting jet in cross flow

Reacting or combusting jets inaugurate some interesting phenomena, which alter the flow field notably. Since solution gas flares operate by introducing a jet of fuel to an oxidizing environment (i.e., cross flowing air), combustion occurs only after the fuel has mixed by molecular diffusion with a stoichiometric amount of oxygen in the air (Majeski 2000). Reacting jets can be classified into two broad regimes: premixed diffusion flames and non-premixed diffusion flames. A single gas or a composition of gaseous fuels, mixed with oxygen before being exposed to a combusting environment, are called premixed diffusion flames (such as Bunsen flames). On the contrary, fuels that do not come in close contact with oxygen before being exposed to the combusting environment are termed as non-

premixed diffusion flames. Most of the gas flaring phenomena in the real world are of the non-premixed class. This thesis will be constrained to discussions of non-premixed diffusion flames.
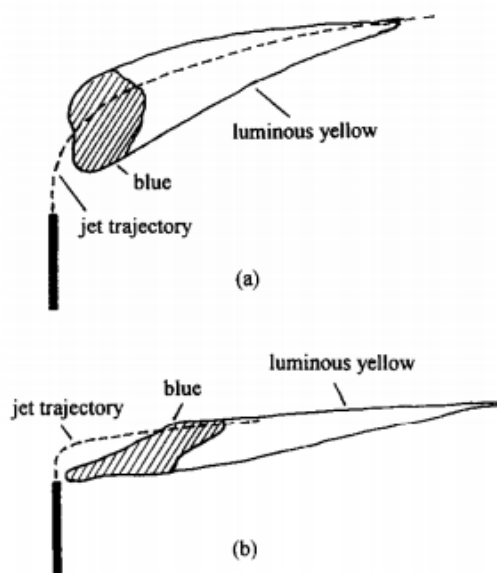
Figure 1.4 : Typical sketches of flames
(a) liftable flame, (b) never-lift flame
(Huang and Chung (1994b)).

Based on the momentum flux ratio (J), the jet flame in cross flow can be classified as either a lifted diffusion flame or a non-lifted diffusion flame(fig. 1.4). Lifted flames appear when the momentum flux ratio is very high. It is noticed that lifted diffusion flames may occur when the flame is ignited below some critical cross flow velocity (U_∞) and then raising the jet velocity (U_j) gradually. On the other hand, when the upstream velocity is higher than a certain value, lifted flames never happen (fig. 1.4). Non-lifted flames are classified into sub-classes (Huang and Chang (1994b)) and denoted as *down-washed, flashing, developing, dual, flickering and pre-blow-off* (fig. 1.5). When the jet-to-wind momentum ratio is very small, and the flammable region is located around the *down-washed*
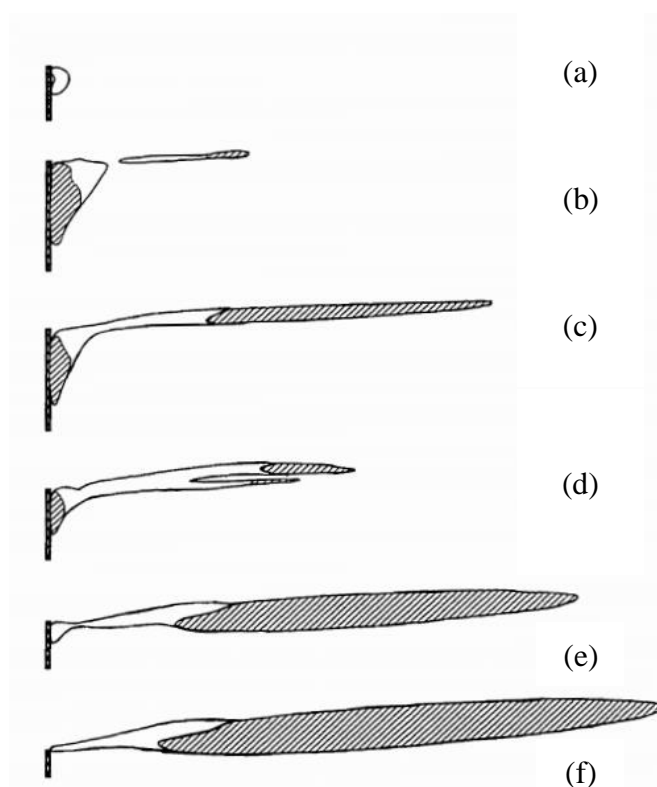
Figure 1.5: The six different flame modes observed by Huang and Chang (1994b): a) down-washed, b) flashing, c) developing, d) dual, e) flickering, and f) pre-blowoff Hatch marks indicate yellow flame and non-hatch marks indicated blue.

recirculation area in the near wake of the tube. The jet body is flushed by the cross stream and curved downward to form a recirculation area due to the down-wash effect around the burner tip area. For a larger velocity ratio, a time-varying intermittent blue flame downstream of the stack is termed as a *flashing flame* and in *developing flames*, this intermittency stabilizes so that a constant axisymmetric flame extends from the wake-stabilized portion, which is shrinking with increased r. Then for a larger jet momentum increases, the flames start shortening and the *dual-flame* patterns appears. The flame

regains its elongation after it reaches the shortest length at which the *dual-flame* pattern is most obviously observed. In flickering flames, the downstream part of the flame begins to flicker and its cross-stream dimension grows. In the end, the small blue flame in the recirculation area disappears and the flame length does not appreciably increase with jet velocity. Just before blow-off, the blue zone anchors to the lee side of the bent jet body above the tip of the burner instead of staying in the wake of the burner. No trace of flame in the recirculation area behind the burner is found (fig. 1.5e). Huang and Chang(1994) modes are descriptive, detailed and well-founded for propane rich fuels. However, the demarcation of the modes is not well defined. Later, Huang and Wang (1999) redefined them in terms of the relative jet and cross flow momenta. Their five modes and range of applicability are: down-wash ($J < 0.1$)) cross-flow dominated ($0.1 < J < 1.6$), transitional ($1.6 < J < 3.0$), jet-dominated ($3.0 < J < 10$), and strong jet ($J > 10$). The later classification is lucid compared to the earlier descriptive classification.

Flame classifications by Gollahalli and Nanjundappa (1995) are relatively simple. They classified the flames into two broad types: type-I and type-II. Type-I flames exist entirely in the downwash zone and type-II flames have two parts, one stays behind the stack and other part exists as an axisymmetric flame. The allocation for these parts depends upon the velocity ratio. Majeski (2000) extended the idea and classified a third type of flame, Type III, which could be identified by the extinction of the wake-trapped part of the flame.

The present investigation is focused on flares having velocity ratios between $0.2 < r < 4$. It may seem more logical to accept the statistical classification of flame given by Huang and Wang (1999) for the flame description of the current study. Although Huang and Wang's experiments were performed in a small wind tunnel, flame imaging done by Majeski(2000) assists in the comparison of the current result with previous results.

1.3.1 Flame trajectory

Previous experimental studies have defined jet trajectories using the local velocity maxima (Kamotani & Greber, 1972) or the local concentration maxima (Smith & Mungal, 1998). This study defines the trajectory from the time-averaged mean flame image. Details are discussed in chapter 3. Trajectories are the physical path of the flame and are an important design parameter when considering the jet fuel concentration (Smith & Mungal,1998).

Scaling parameters are those parameters which helps to collapse the trajectory path (while normalized) for different crossflow and jet velocity. Empirical equations for the jet in cross flow trajectories were first given by Pratte and Baines (1967) for the non-reactive jet in crossflow. Trajectory results collapsed at rd(velocity ratio times diameter) scaling in their study. The velocity ratios were in the range of 5 to 35. Meanwhile, a previous study of jet trajectories by Keffer and Baines (1963) also collapse with Jd(momentum ratio times diameter) scaling when momentum ratio, $J \geq 6$. More recent studies carried by Su and Mungal (2004), Mupiddi and Mahesh (2005), New et al. (2006) also show that rd scaling providess a better collapse of crossflow trajectories. These studies are based on cold jets.

Flame trajectories given by Holdman (1976) provide a better indications that there are no significant difference in reactive jet trajectories and non-reactive jet trajectories at high velocity ratios. Later Muniz and Mungal (2001) found that that heat release altered the velocity field, but the overall jet trajectory remained quite similar to the nonreactive analog at high momentum ratio. At low velocity ratios, the buoyancy effect induced by the flame causes the flame trajectories to deviate from the established empirical equations. A list of empirical equations for jet in crossflow is given in table 1.1.

Table 1.1: List of the empirical equation for the trajectory:

Author	Empirical equations	Ratios	Constant value
Pratte and Baines (1967)	$\dfrac{y}{dr} = A\left(\dfrac{x}{dr}\right)^{B}$	r = 5-35	A = 2.05 B = 0.28
Smith and Mungal(1998)	$\dfrac{y}{dr} = A\left(\dfrac{x}{dr}\right)^{B}$	r = 5- 25	A = 1.5 B = 0.27
J R Holdman (1976)	$\dfrac{y}{d\sqrt{J}} = A\left(\dfrac{x}{d\sqrt{J}}\right)^{B} J^{C} s^{D}$	J = 5 - 60	A = 0.76, B = 0.27, C = 0.155, D = 0.15

1.3.2 Flame length (L_F)

Prediction of the size and shape of the flame in a cross-wind is an important parameter for engineers to design flare stacks. In 1928, Burke and Schumann were the first to report quantitative measurements on diffusion flames in a quiescent environment. Later, Gollahalli et al. (1975), Huang and Chang (1994b) Huang and Wang (1999) performed their experiments to measure flame length using visible flames or the Schlieren technique for long exposure photographs. Kalghatgi (1983) used a similar approach in his measurements but instead of using long exposure images, he recorded a video (seemingly 30fps, shutter speed 1/60s). Kostiuk et al.(2000) provided the concept of determining the flame length statistically by the probability of flame occurrence, which accounts for the relatively large fluctuation of flame size and shape (fig. 1.6). Kostiuk et al.(2000) defined the flame length as the linear distance between the flame tip and the centerline of the stack

exit at the 10th percentile contour. Later, Majeski(2000) proposed a compressive model to predict flame length at low velocity ratios for propane rich fuels.
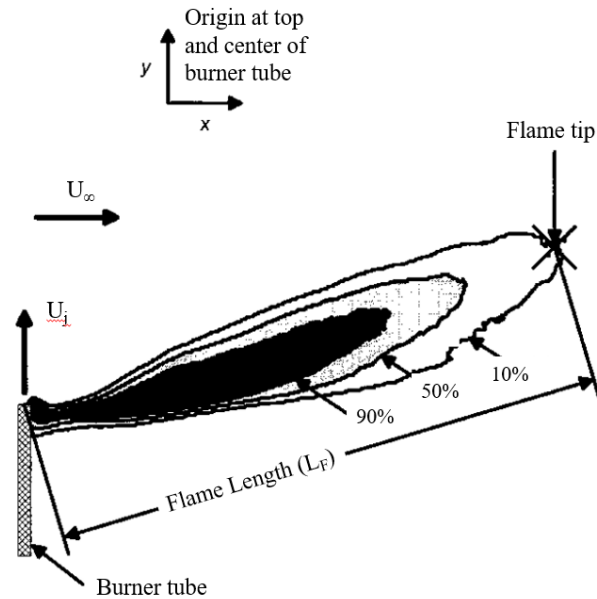
Figure 1.6: A mean propane flame image created by averaging 200 instantaneous images where the jet exit velocity is 1 m/s and the transverse air velocity is 2 m/s. (Kostiuk et al., 2000).

More recent experimental studies (Wang et al., 2015; Shang et al., 2017; Tao et al., 2018; Xin et al., 2018) suggest considering all the images to process for predicting flame length. Wang et al. (2015) used the Otsu (1979) technique for image binarization (a process of converting a pixel image to a binary image to extract desired feature) which does not seem like a good solution at all. The technique is used for conventional real world image processing. Details are discussed in chapter 2 and Appendix A. In this study, the concept of Majeski (2000) is taken and extended to filter the noise and automate post-processing for all sequential images by developing a code specifically to get binarized images and overall to measure the flame length (L_F).

1.4 Flaring efficiency (η)

Flaring efficiency or carbon conversion efficiency is an important feature for large scale gas flaring exposed to an open environment. Eqn. 1.4 represents the global combustion reaction. For complete combustion, the carbon molecule in hydrocarbon (C_xH_y) is completely converted to CO_2. Eqn. 1.5 represents the definition of flaring efficiency.

$$C_xH_y + aO_2 = bCO_2 + dH_2O + eCO + fCH_4 + \sum_{m,n} g_{m,n}C_xH_y \qquad 1.4$$
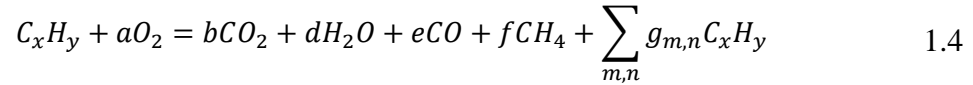
$$\eta = \frac{\text{mass accumulation rate of carbon in the form of } CO_2 \text{ produced by the flame}}{\text{mass flow rate of carbon entering the flame in the form of hydrocarbon fuel}} \qquad 1.5$$

Johnson and Kostiuk(2002) explained the wind tunnel methodology and determine the flaring efficiency. Figure 1.7 represents the crossflow velocity effect on flaring efficiency(η) for a wide range of crossflow velocities (2m/s – 14m/s) and a single jet velocity (3m/s). From the figure, it is clear that conversion inefficiency increases with the increase of mean crossflow velocity. In addition to that, the turbulent cross-wind increases the carbon conversion inefficiency more than laminar cross-wind. The increase of carbon conversion inefficiency raises the possibility to form carbon

Figure 1.7: Effect of added ambient turbulence in the cross-wind on the inefficiency of a natural gas flare(Johnson and Kostiuk, 2002).

mono-oxide, the existence of methane or unburned hydrocarbon. Interestingly, flaring

inefficiency increased when the crossflow is turbulent instead of laminar. However, Johnson and Kostiuk(2002) provide no details of the turbulence condition, so the experiment is difficult to interpret. The effects of turbulence are one of the prime issues examined in this thesis.

1.5 Current study

To generate turbulence at the wind tunnel, roughness block, barriers, spires, and grid are generally used. In the current study, a grid is used to generate atmospheric turbulence because it is comparatively easy to control turbulence parameters using grids. Two parameters are important to discuss turbulent flow: turbulence intensity (I_u) and integral length scale (L_x).

Turbulence intensity is defined as the ratio of the standard deviation of the velocity fluctuations (u') to mean velocity ($\bar{u}$) (eqn. 1.6).

$$I_u = \frac{\sqrt{\overline{u'^2}}}{\bar{u}} \qquad\qquad 1.6$$

Integral length scale, L_x can be estimated from the autocorrelation coefficient $\rho(\tau) = R_{uu}(\tau)/(u'_{rms})^2$, where,

$$R_{uu}(\tau) = u'(t)\, u'(t+\tau)\, d\tau \qquad\qquad 1.7$$

In equation 1.7, $R_{uu}(\tau)$ represents the autocorrelation function, and τ is the time lag. In this case $L_x = UT_x$ where T_x is the integral time scale, obtained from the area under the $\rho(\tau)$ curve.

$$L_x = \bar{u} \int_0^\infty \frac{R_{uu}(\tau)}{\sigma_u^2} d\tau \qquad\qquad 1.8$$

In addition to statistical analysis, the integral length scale has a significant physical meaning. It is assumed that turbulent flow has been carried by numerous numbers of eddies having different size. The integral length scale represents the physical size of the eddy that contains a significant amount of energy. In the next section physical characteristics of grid turbulence, corresponding energy spectra are described in detail.

1.5.1 Grid turbulence

Grids are of 2 kinds: active grid and passive grid (fig. 1.8). I_u and L_x are controlled by changing of stepper motor rpm and winglet angle for active grid. Passive grid is comparatively simple to operate. By changing the bar thickness (b), bar to bar distance (M) and relative position of the grid to test section. Because of geometric complexity and expanse passive grid is the ultimate choice over the active grid for wind tunnel experiments.
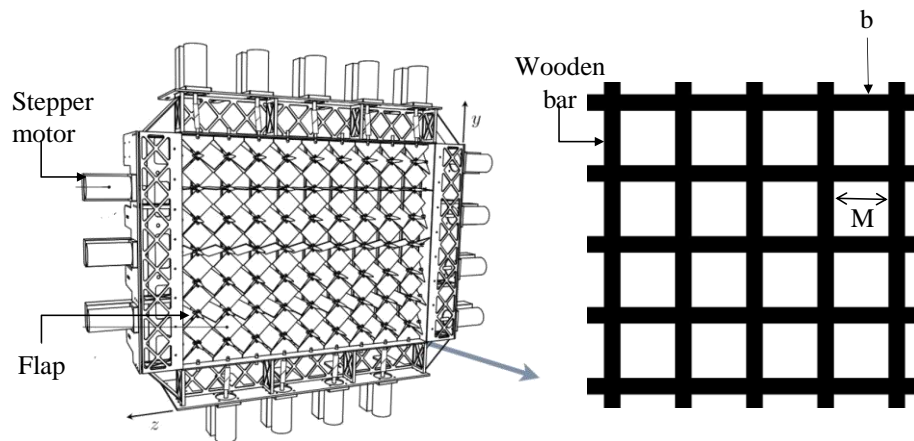
Figure 1.8: Physical representation of active (Wiley, 2019) and passive grid.

The flow downstream undergoes a series of transitions & develops a wake region behind the bars. Rapidly evolving vortices are shedding downstream which eventually form a fully developed turbulence field (Vita et al., 2018). The effect of the grid on the flow field may be separated into two parts: manipulation effect and wake effect (Roach, 1987). The manipulation effect consist of processes whereby the spectrum of turbulence is altered, reducing or increasing the scale of the upstream turbulent eddies according to the

dimensions, relative to the grid. The wake contributes to transport of turbulent energy in the downstream flow, this is at a high relative frequency and so decreases the scale of upstream turbulent eddies. Both of the effects act in a complex manner to produce homogeneous flow.

The generated turbulence kinetic energy is found to decay rapidly with increasing downstream distance from the grid. It is found that the level of turbulence kinetic energy generated is directly proportional to pressure drop (Roach, 1987) due to the drag. The drag force causes mean velocity gradients downstream of the grid. Laneville (1973) and Vickery (1966) suggest keeping the coefficient of drag, C_D less than 2(where, $C_D = \frac{b/M(2-b/M)}{(1-b/M)^4}$). The higher C_D results in higher initial turbulence production and, therefore, higher dissipation of turbulence downstream of a grid (Sarkar and Savory, 2019).

The co-efficient of drag depends upon the bar to mesh size ratios of the grid (as indicated earlier (Hinze, 1959)). The rigidity ratio (b/M) is suggested to be set 0.125 to 0.29 (Vita et al., 2018; Vickery, 1966) and the thickness ratio (t/b) is suggested to be set to about 0.2. The ratio b/M can be chosen based on the definition of grid drag (Laneville, 1973).

Experimental studies have been conducted to determine the relationship of turbulence intensity, length scale with grid geometry. Nakamura and Ohya(1983), Roach(1987), Tornado et al.(2015), Vita et al.(2018), Sarkar and Savory(2019) established the geometric parameters to quantify I_u and L_x. The equations differ from one another as grid turbulence is not independent of wind tunnel configuration. Nakamura and Ohya(1983) conducted an experiment in a uniform cross sectional tunnel configuration. Whereas, Roach(1987) and Vita et al.(2018) did their experiments in a slightly converging cross-sectional tunnel. Large wind tunnels always have background turbulence, which would affect the results. The literature tends to lack the information regarding the background turbulence from the above-mentioned authors. The cross-sectional thickness of the grid might play a role in determining the mathematical relations which is also absent in many studies. The empirical relations are described in Table 1.2 :

Table 1.2: Empirical relations for grid turbulence parameters

Author name	Intensity	Length scale	Constant value
Vickery(1966)	$I_u = A \left(\frac{x}{b}\right)^{-\frac{5}{7}}$	$L_x = C \left(\frac{x}{M}\right)^{0.84}$	A= 1.12, C = 0.075
Roach(1987)	$I_u = A \left(\frac{x}{b}\right)^{-\frac{5}{7}}$	$L_x/b = C \left(\frac{x}{b}\right)^{\frac{1}{2}}$	A = 1.13, b = 0.89, C = 0.2
Sarkar and Savory (2019)	$I_u = A \left(\frac{x}{b}\right)^{-0.72} \left(\frac{x}{M}\right)^{-0.07}$	--	A = 1.49

Sarkar and Savory(2019) introduce both M and b to quantify turbulence intensity, which is different from other mentioned authors and seemingly more accurate as intensity should not be only a function of bar thickness (b).

1.5.2 Energy spectrum
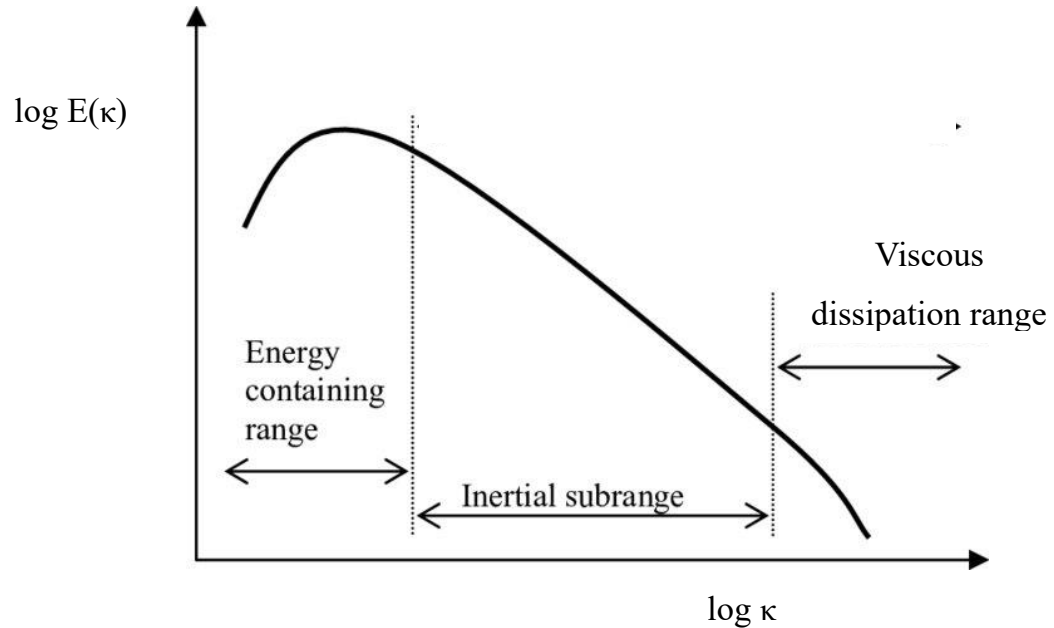
Figure 1.9: Energy spectrum of turbulence for cross-wind (Hjertager, 2014).

A turbulent flow contains energy across a wide range of wave numbers ($\kappa = 2\pi f/U_{mean}$, where f is the frequency). Fig. 1.9 represents the energy spectrum of turbulent crossflow. The wave number (κ) is inversely proportional to the eddy diameter (Davidson, 2014). Fig. 1.9 indicates that the energy of eddies varies with the eddy size. Larger eddies contain more energy and smaller eddies contain less turbulent energy. The energy spectrum can be divided into three different region.

I.   Large energy containing eddies: Large eddies carry most of the energy. These eddies interact with the mean flow and extract energy from the mean flow. The energy extracted by the largest eddies is transferred to slightly smaller scales.

II.   Inertial subrange: The eddies in this region represent the mid-region. The turbulence also tends to be isotropic in this region. Energy is coming from the lower part of the energy containing range to the upper part of the viscous dissipation range.

III.   Viscous dissipation range: The energy transfer from turbulent kinetic energy to thermal energy. The scales of the eddies in this range are described by the Kolmogorov scales.

The Von Karman equation (eqn. 1.9) provides an empirical form of energy spectra over the complete frequency range applicable for grid turbulence of the atmospheric boundary layer (ESDU 85020) as well. The normal form of the Von Karman spectral equations is :

$$\frac{f S_{uu}(f)}{\sigma_u^2} = \frac{4 \, f L_x / u_{mean}}{(1 + 70.8 \, (f L_x / u_{mean})^{\,2})^{5/6}} \qquad\qquad 1.9$$

where, σ_u and $S_{uu}(f)$ are the standard deviation and power spectral density of the crossflow velocity fluctuations, respectively. In the current study, the axis of the spectra is normalized using the mean velocity (u_{mean} or U_∞) and the internal diameter of the flare stack (d), rather than σ_u and L_x. So that the effects of turbulent intensity is included in the plot along with the size of the energy containing eddies relative to the flare stack diameter. A comparison of real world atmospheric boundary layer turbulent spectra along with wind tunnel spectra are discussed in detail in chapter 2.

1.6 Objectives and approach

The purpose of this investigation is to systematically study the turbulence effects on gas flares. The hypothesis motivating this work is that turbulence may affect the efficiency, based on a single, uncontrolled study of Johnson and Kostiuk (2002). Real world turbulence in a reduced scale will be developed in a wind tunnel to assess this hypothesis. Sequential colour images of flares, taken for different turbulence conditions, allow us to achieve insight into wind turbulence effects on gas flares. The analysis will be performed on a wide range of velocity ratios ($0.2 < r < 4$) which will make a comparative relation between reactive and non-reactive jets in crossflow. Additionally, some experiments are conducted at very low turbulence intensity ($I_u < 1\%$) to compare smooth flow to turbulent flow. A direct comparison will be made for nearly laminar (smooth) to a highly turbulent condition, which will acknowledge the necessity to conduct flaring experiments for turbulence background. Flame length and flame trajectory are measured for this wide range of momentum ratios under different turbulence condition. Ultimately, the goal is that these findings will help to reduce emissions from flare stacks.

A square mesh bi-planer grid is used to generate turbulence. High frequency velocity data quantify turbulence parameters using hot wire anemometry and Cobra probes. Colour cameras are used to map the flare geometry. Chapter 2 deals with the experimental set-up and methodology. The scaling of the model and wind simulation will be described along with details of the method of analysis. Chapter 3 will discuss the analysis of the flame length and flame trajectory results. Chapter 4 will discuss the effect of turbulence on flames. Conclusions and recommendations are discussed in Chapter 5. Image processing techniques and uncertainty analysis are discussed in Appendix A and B, respectively.

Chapter 2

2 Methodology and Analysis Procedure

In this chapter, the experimental set up is explained in section 2.1. Details pertaining to the measurement devices, and the physical set-up are described in detail in this section. Characteristics of flow measurement and image acquisition parameters are described in section 2.2. The wind tunnel flow field is discussed in section 2.3.

2.1 Closed loop wind tunnel details and flare geometry

The experiments were performed in the closed-loop Boundary Layer Wind Tunnel II at the University of Western Ontario (Fig. 2.1). There are two test sections: one on the high speed side and the other on the low speed side of the wind tunnel. The current study was performed in the low speed side where the maximum speed is 11 m/s. However, during the experiments, the maximum cross-wind speed was kept at or below 10 m/s. The tunnel is run by a 289 hp motor placed at the downwind side of the high speed test section.
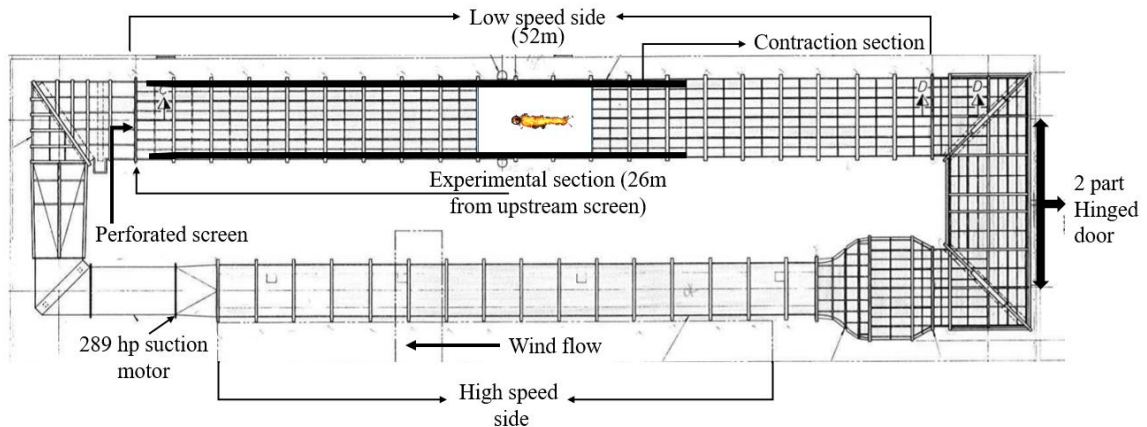
Figure 2.1: Top view of the Closed Loop Wind Tunnel.

The pressure on the low speed side is slightly higher than the atmospheric pressure when the wind tunnel is running. The total length of the low speed side is 52m. At the inlet of low speed side, there is a perforated screen. The screen is placed to control the turbulence

entering the test section. A stack was placed 26m downstream of the screen. At this position, the test section is 3.6m high. A contraction section was added into the existing section to improve the inlet flow quality (fig. 2.1). The width of the test section is 3.65m, narrower than the usual 4.88m because of the presence of the contraction. The 2 part hinged door (fig. 2.1) is opened after every 4 sets of experiments to blow out the exhaust products of combustion. Measurements of hydrocarbon and combustion products are taken before starting new set of experiments.
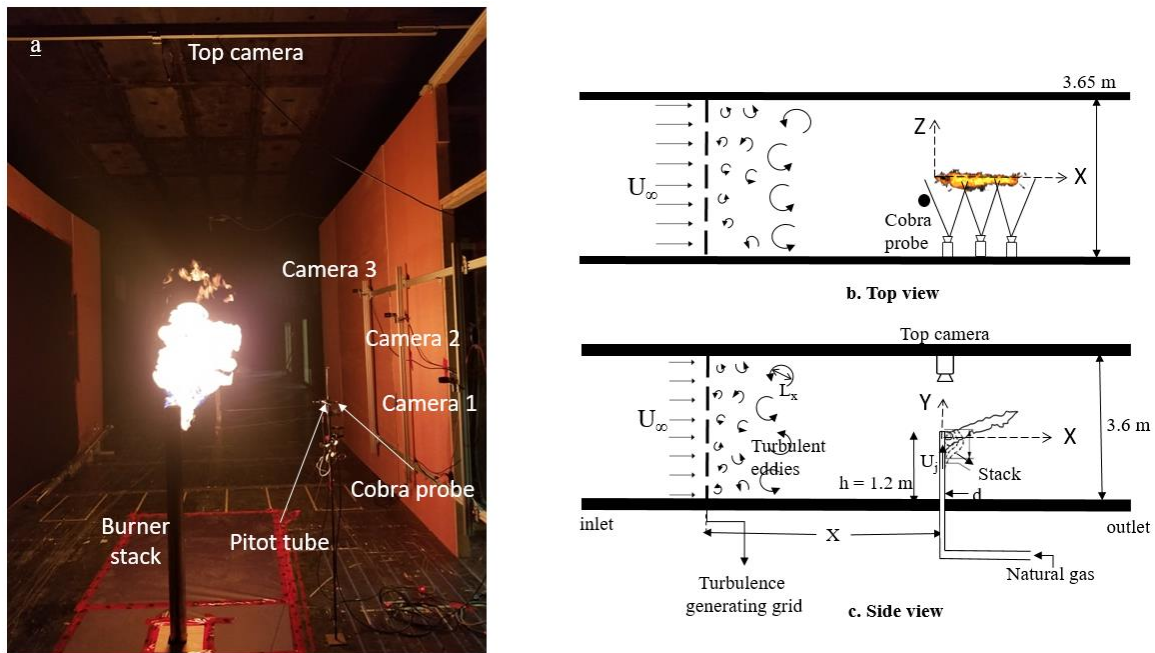
Figure 2.2. (a) A physical representation of the measurement devices and their positions, and a schematic of the experimental setup from the (b) top, and (c) side.

Figure 2.2a provides a photograph of the experimental setup, showing the relative location of the burner stack, Pitot-static tube, Cobra probe, the cameras. The overview of the experimental setup (as schematic) is provided in figure 2.2(b,c). In addition to basic definitions, the coordinate system and the geometry are provided. Details will be discussed in the following section.

Based on crossflow characteristics, the experiments were labelled as cases: A, B, and C. Where, case A represents nearly laminar (smooth) flow ($I_u < 1\%$), case B is moderate turbulence level ($I_u = 3.72\%$, $L_x = 0.32$m) and case C represents high turbulence level ($I_u = 5.78\%$, $L_x = 0.23$m).

2.2 Apparatus and test parameters

2.2.1 Velocity measuring apparatus

A Pitot-static tube was used to measure and control the wind tunnel velocity. It was placed at several positions both upstream and downstream of the stack.

The Cobra probe is a dynamic multi-hole pressure probe for measuring mean and fluctuating 3-component velocities and static pressures. The Cobra probe can take time-varying velocity samples at up to 1250Hz rate. The Cobra Probe is robust and withstands moderate knocks and contaminated flows. It comes fully calibrated and does not need recalibrating other than occasional checking of the voltage-to-pressure scaling (static calibration) to ensure it is functioning accurately. Further details can be found in TFI catalogue (2019).

Hot wire anemometers use a fine wire (on the order of micrometers) electrically heated to some temperature above the ambient. Air flowing past the wire cools the wire. The rate of cooling is proportional to the wind velocity, which is the basis for this commonly used device.

One of the advantages of using the hot wire probe is that it can measure velocity fluctuation at much high frequencies than the Cobra probes. Additionally, velocities lower than 2 m/s could be accurately measured using hot wire anemometer. However, Cobra probes provide all three velocity components, which is much more difficult to do with hot wires (only single wires were used in the current study).

2.2.2 Gas composition and flow controller

The fuel mixture to be tested is a six-component mixture of methane, ethane, propane, butane, nitrogen, and carbon dioxide representative of sample composition data from the upstream oil and gas industry (Conrad and Johnson, 2019). The flare gas compositions are derived from median Alberta Energy Regulator data (2016). The fuel flow rate was controlled by Bronkhorst mass flow controllers. The gases are kept in cylinder separately outside the wind tunnel and the mass flow controller is used to maintain the proper gas composition ratio. Details of the gas flow system are shown in fig. 2.3.

a - Two stage pressure regulator

b - Bronkhorst mass flow controllers

c - Gases coming through holes in the burner base

d - Multiple fine screens for homogenize the

   gas mixture

e - Uniform jet mixture
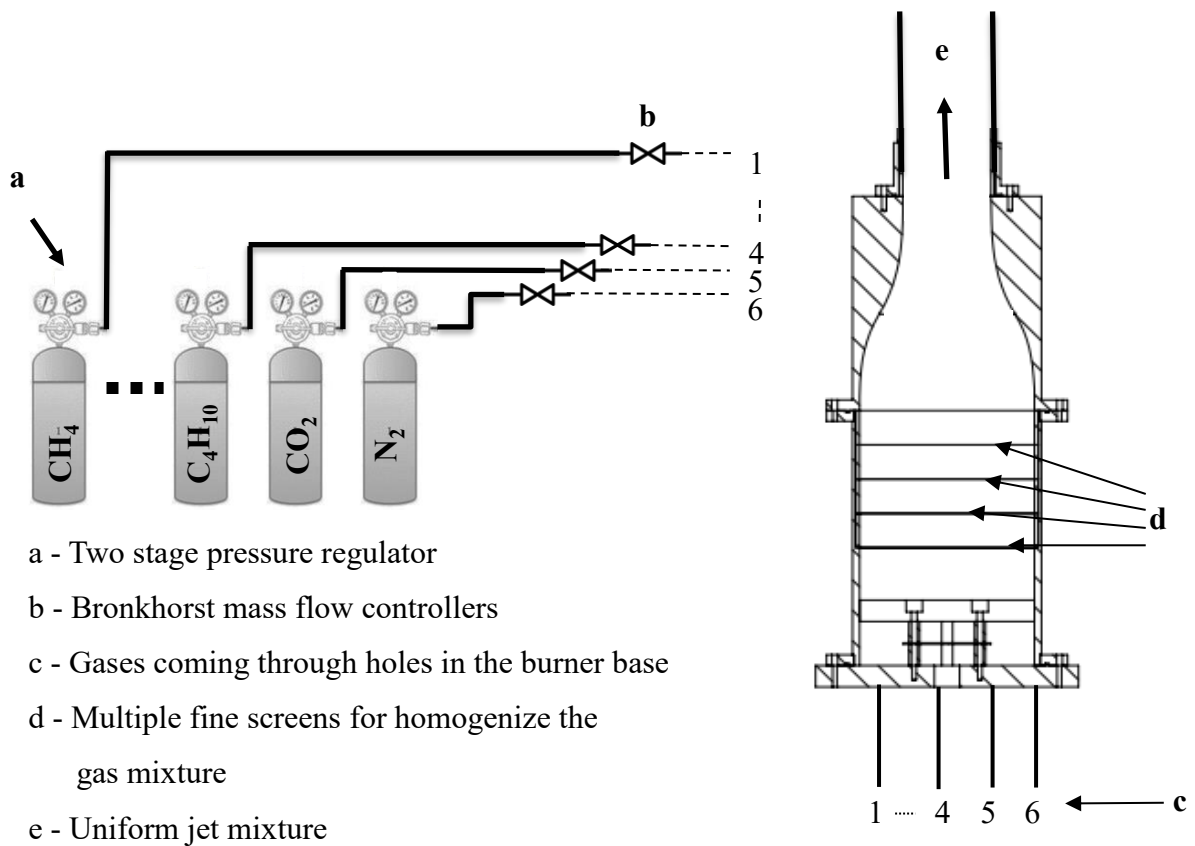
Figure 2.3: A schematic representation of flare gas supply system.

The gas supply system is designed and built by Mr. Darcy Corbin, research engineer of FlareNET strategic network. Based on the nozzle diameter, the fuel flow rate was set such that the required jet velocity can be achieved. The temperature in the wind tunnel is

considered to control the gas mixture flow rate. The flare gas composition is given below in table 2.1.

Table 2.1: Flare Gas Composition

Species	Volume Fraction (%)
Methane, CH_4	86.03
Ethane, C_2H_6	6.81
Propane, C_3H_8	2.35
Butane, C_4H_{10}	1.99
Nitrogen, N_2	1.61
Carbon Dioxide, CO_2	1.21

2.2.3 Burner Details

The flare tips are designed based on the dimensions of a 1" NPS SCH 40[1] pipe with an outside diameter (OD) of 1.173" (29.78 mm), a wall thickness of 0.124" (3.149 mm), and an inside diameter (ID) of 1.049" (26.64 mm). These dimensions yield an ID/OD ratio of 0.8947 which will be held constant across the other burner sizes. The 2" and 3" NPS SCH 40 pipes in which the other burner sizes were manufactured with inside diameters as shown in Table 2.2 and have outside diameters machined to match the required ratio.

---

[1] NPS SCH 40 represents Nominal Pipe Size Schedule standard. Numeric value 40 indicates the wall thickness of the pipe based on standard.

Table 2.2: Flare stack diameters

Nominal Diameter (in)	Flare ID (in (mm))	Flare OD (in (mm))
1	1.049 (26.64)	1.173 (29.78)
2	2.067 (52.50)	2.310 (58.68)
3	3.068 (77.93)	3.429 (87.10)

2.2.4 Passive Grid

Three parameters are important to design a grid to generate the desired turbulence: the width of the bar (b), the mesh size (M), i.e., the distance between centerline distance of the bar, and the downstream distance (X) from the grid to where the measurements are taken. Vickery (1966) provides an indication for the optimal mesh size of M = L/8, to get homogenous turbulence at the experimental section (where L is the length of the test section). The ratio b/M can be chosen based on the definition of grid drag (Laneville, 1973) which is discussed in section 1.1.4. Based on the physics of grid turbulence, the bar size was 0.1016m (4 inch) and mesh size was 0.508m (20 inches). It was a bi-planer square grid (fig. 2.4).

The grid was positioned in two different position upstream of the flare (19.2M and 40M, where, M bar to bar distance). The grid is made of wood. To provide sufficient stiffness 4 L-shaped metal plates were screwed vertically and 1 metal plate was screwed at top horizontally. The grid covered the entire wind tunnel cross-section.
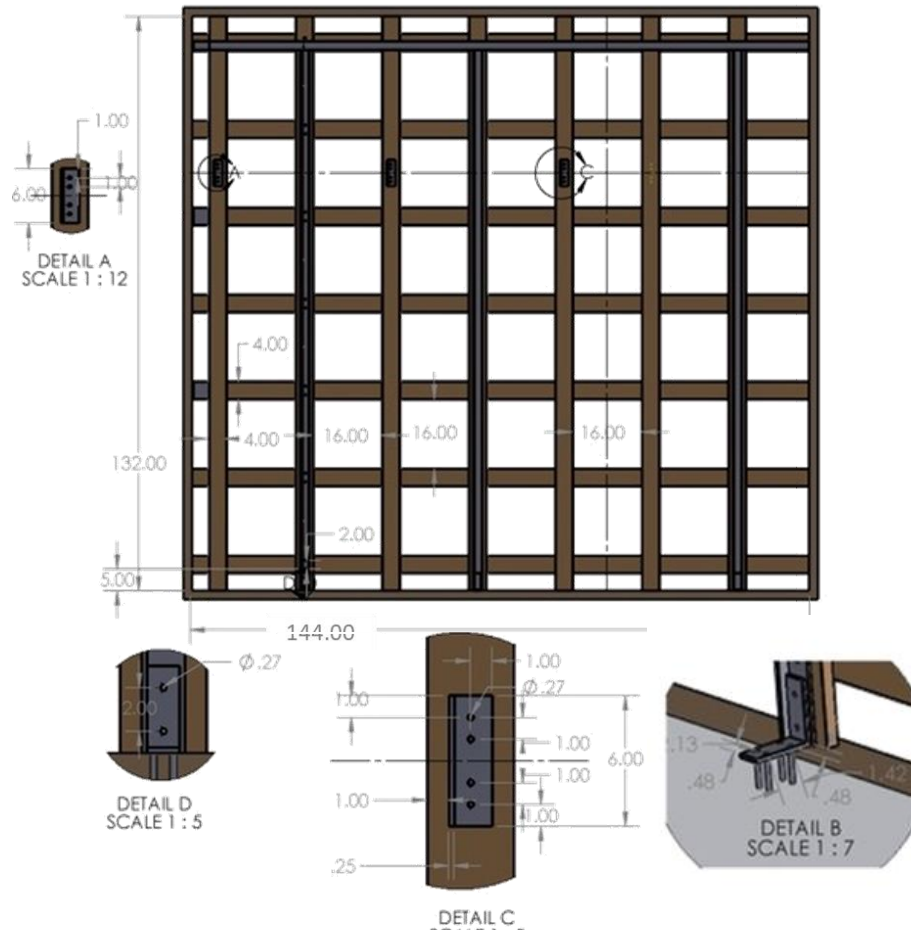
Figure 2.4: A Schematic drawing of the turbulence generating grid (dimensions in inch).

2.2.5 Camera sensor characteristics

To visualize the flame, multiple high frame rate cameras were used. Since it was not possible to capture the whole flame with high resolution using one camera, multiple cameras were required. In total, three cameras were placed side by side to map the whole flame. An additional camera was placed at the top to capture the near field from the top (simultaneously with side images) to depict the flow topologies under different conditions (presented in table 2.3). The camera specifications are described in table 2.4. Area covered

by a single camera increases with distance from camera and test section. Fig. 2.5 represents frame area for single camera vs distance from camera to experimental section.

Table 2.3: Physical configuration of the camera

Camera model	Basler Aca 1920 (Sensor: Sony IMX 174)	
No of cameras	4	Three cameras for capturing whole flame length from side and one for capturing flame from the top
Lenses	17 mm	To use to capture full flame length from side
	28 mm	To capture image from top
Distance from flame	1.8m (approx. from side and from top)	Field of View: $1.2m^2$ (horizontal = 1.271m, vertical= 0.8m)

Table 2.4: Specification of the camera sensor

Camera name (Sensor name)	**Basler acA 1920 (Sony IMX 174)**
Resolution (pixels)	**1920*1200**
Pixel size(µm)	**5.86**
Frame rate (images/sec)	**155**
Saturation capacity (e^-)	**32513**
Dynamic Range(Decibel)	**12.18**
Signal to noise ratio(SNR)	**7.5**
Colour	**RGB**
Quantum efficiency	**76%**
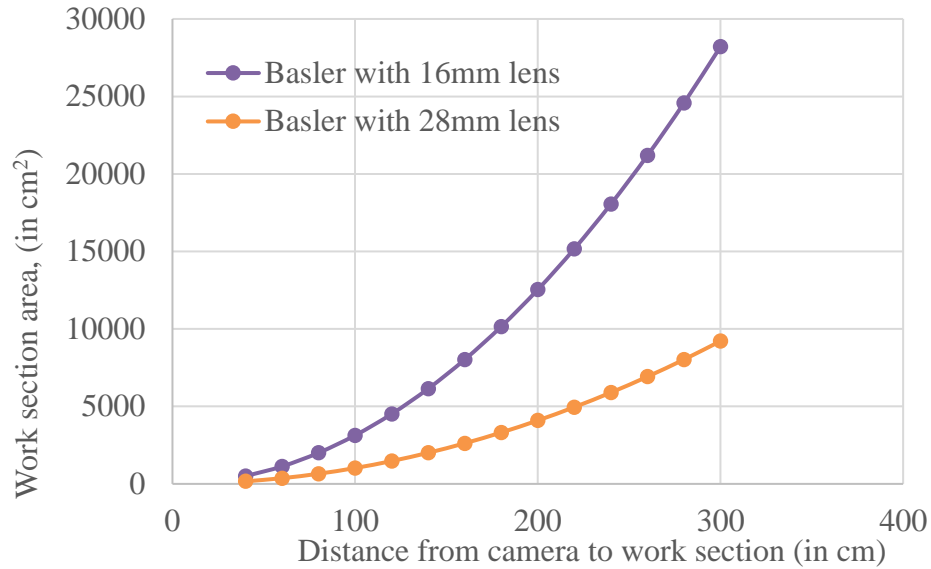
Figure 2.5: Representation of Frame area vs distance from camera.

2.2.6   Image acquisition technique

The imagary is captured using commercial software (Norpix 3.7) and LabVIEW 19.1. A developed visual interface (VI) of LabVIEW is attached with a brief explanation in Appendix A. No hardware triggering device is used to take the images. Rather, software triggering is used to take the images simultaneously. Approximate time lag between the 1st camera image and the 2nd camera image is 4ms (millisecond), 1st to 3rd is 9 ms and 1st to the the camera is 7ms.The general image acquisition parameters are kept the same for all four cameras. The focal length of the lenses are 17mm. Further details are provided in Table 2.5.

Table 2.5: Image acquisition parameters

Camera attributes	Values
Exposure	0.0005 sec
Frame rate	50fps(Commercial software) 30fps (LabVIEW VI)
Image type	Tagged Image Format (.tif)
Compression	Uncompressed
Bit depth	8
Colour channel	RGB
Image acquisition duration	60-75 sec

2.2.7   Image processing technique

Image processing is a major part of this work. The images in the current study can be viewed as 3D matrix where Red, Green, and Blue represents the three-dimensions simultaneously. Each dimension is a 2D matrix having 1920*1080 values for a single image. There are several issues in image processing which needs to be addressed. First, the goal was to map the entire flame, while images are taken from the side using three separate cameras. A 10% to 15% overlap between the cameras is used to identify the entire flame. Details of how the overlap is considered are provided in Appendix A.

A second issue is image binarization. To get the flame length and flame centerline trajectory, it is essential to binarize the sequential images. After the boom of the digital fast image acquisition technique after 2000, most of the authors in the field of jet in cross flow used Otsu's method (1979) to binarize the sequential image. Otsu's method is applicable for real world day to day imaging and it give excellent result when binarizing wide range of image data. However, the build-in command for Otsu's method can't help to depict the true scenario. A modified algorithm is added at appendix-A.

2.3   Flow field and jet details

2.3.1 Velocity and momentum ratios

The test was conducted using 1-inch nozzle at 5 different cross flow velocity: 2, 4, 6, 8, 9.5 m/s and 4 jet velocities 2, 4, 6, 8 m/s. So, the total combination was 20 for each case. The total test case was 20*3 = 60. The velocity ratio (U_j/U_∞) range was 0.2 to 4. The density of the fuel mixture is 0.79 kg/m^3. The Reynolds number range is 3340 to 16000 for the crossflow and 3800 to 15200 for the jet based on diameter of the stack. Momentum ratios are listed in table 2.6 for different velocity condition.

Table 2.6: Momentum ratio of flows

Momentum ratio		U_j(m/s)			
		2	**4**	**6**	**8**
U_∞(m/s)	**2**	0.66	2.63	5.91	10.51
	4	0.16	0.66	1.48	2.63
	6	0.07	0.29	0.66	1.17
	8	0.04	0.16	0.37	0.66
	9.5	0.03	0.11	0.24	0.42

The velocity condition was applied for all three turbulence cases mentioned in section 2.1. Some experiments were also carried out for a 2-inch diameter nozzle and 3-inch diameter flare stack to observe flame length which is discussed in the results section.

2.3.2 Wall boundary layers and flow uniformity

Measurements has been taken to determine the vertical and lateral velocity uniformity. Fig. 2.6 illustrates the mean streamwise velocity (U/U_∞) profile above the wind tunnel floor at different flow conditions. The crossflow velocity reaches free stream velocity or within

95% of free stream velocity at 60cm height from the ground. The burner exit is kept 1.2m height from the wind tunnel floor. So, there is no effect of the boundary layer acting on the flame, although there will be effects on the lower portion of the stack (as there would be in full-scale).
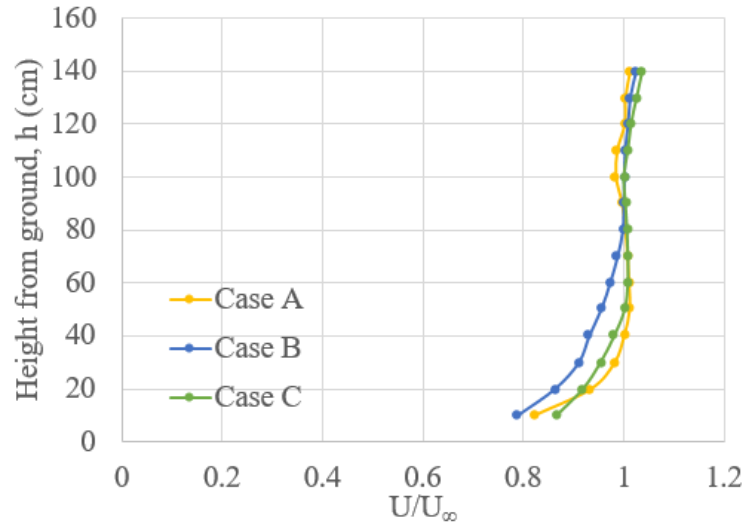
Figure 2.6: Variation of velocity at different height (fan speed 6V).

Fig. 2.7 shows mean streamwise velocity in lateral direction. The figure indicates a uniform crossflow velocity in lateral direction for case A, case B, and case C. Velocity measurements are taken at 1.2 m height, and from center plane to 1.3 m on both side. Crossflow velocities at different position deviate 5% to 10% from the mean freestream velocity. The deviation of velocity from free-stream velocity is comparatively higher near the wind tunnel wall and uniform at the center plane of wind tunnel.
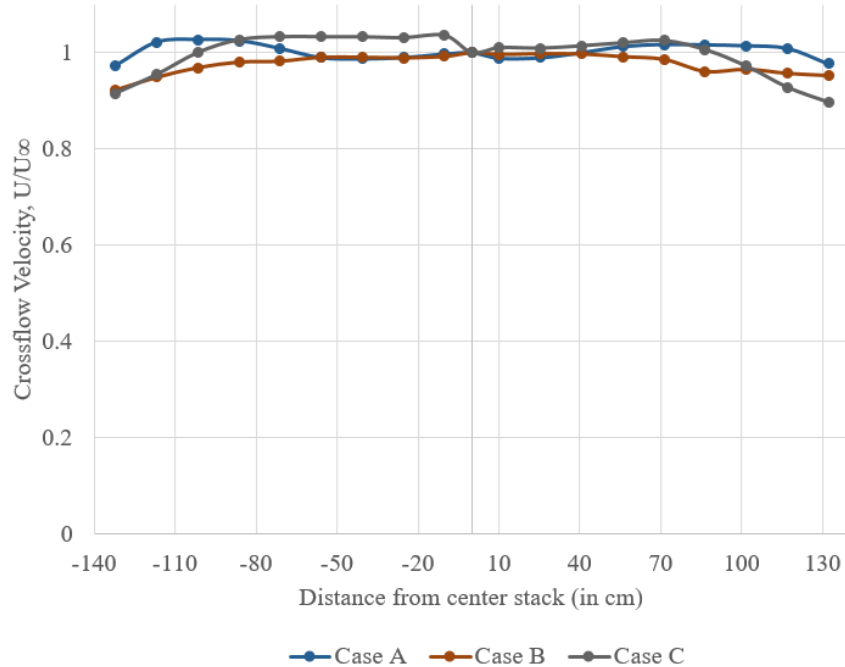
Figure 2.7: Velocity variation from the center plane in lateral direction (wind tunnel fan speed at 6V).

2.3.3   Grid turbulence data

The results presented in this section consider the following topics of investigation: the relation of (i) turbulence intensity and (ii) length scale with increasing downstream distance from the passive grid. The current experimental results are also compared with previously published results.

In fig. 2.8, the I_u is plotted against x/M, showing its decay as a function of downstream distance. In this case, the experimental results behave consistently with previously published results at x/M = 10, 19.2. However, turbulence intensity value at 40M downstream is little higher than the empirical relations. This indicates that decay of turbulence is slower in experimental cases.
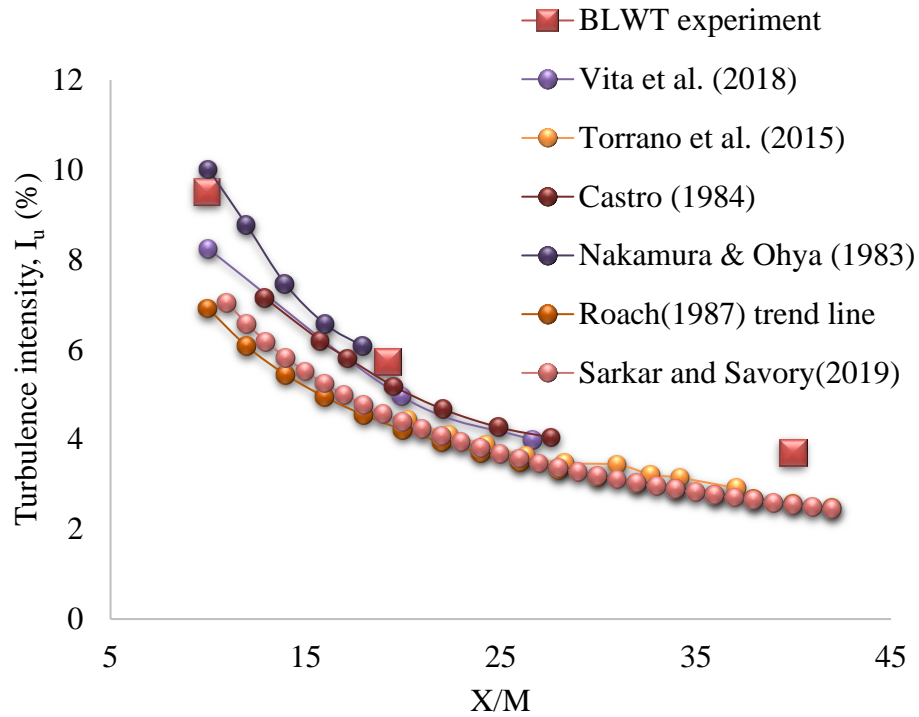
Figure 2.8: Comparison of turbulence intensity vs downstream distance (x/M).

In fig 2.9, integral length scales are plotted against x/M. In the plot, the integral length scales are non-dimensionalized by the bar width (b) of the grid. The length scale (L_x) increases with increasing downstream distance. The current experimental results indicate that length scale falls in between the previously published result (Torrano et al., 2015) and empirical relation (Roach, 1987)
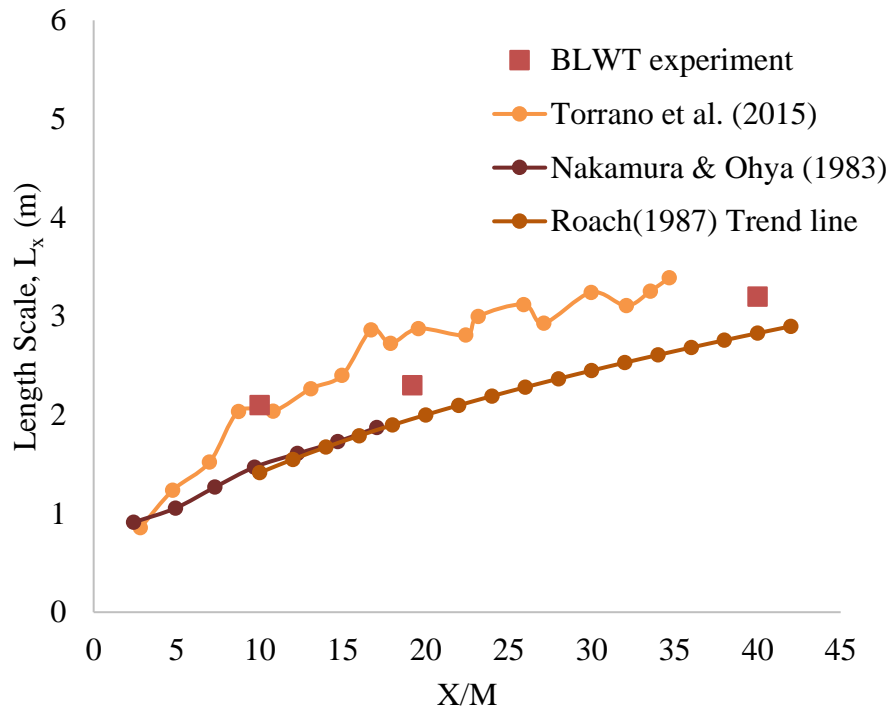
Figure 2.9: Relation between non-dimensional length scale vs downstream distance (x/M).

2.3.4 Energy spectra

Time series of velocity were obtained during the experiments using a hot-wire anemometer and Cobra probes. Hot wire anemometry is superior for high frequency measurements and the hotwire used in the experiments can take up to 10000 samples/second. The velocity time histories were converted to frequency (f) domain using FFT (Fast Fourier Transform). $S_{uu}(f)$ represents turbulent kinetic energy distribution in the frequency domain. For a wide range of frequency, a wide range of energy is obtained. This energy band is called an energy spectrum for turbulent flow. The energy spectrum was obtained using this technique during the experiments. However, to get the full scale energy spectrum (from ESDU, 85020), a normally used forms of the von Karman spectral equation is:

$$\frac{f\ S_{uu}}{\sigma_u^2} = \frac{4f_u}{(1+70.8f_u^2)^{\frac{5}{6}}}$$

2.1

where, $f_u = f.L_x/U$, L_x is the integral length scale of the flow (section 1.1.4), σ_u is the standard deviation of fluctuating velocity, U_∞ denotes mean wind speed. The inner diameter (d) of the 1 inch burner stack is used to normalized the experimental spectra. To obtain the range of possible full scale scenario, streamwise turbulence intensity was set to 15% to 20% (figure 1, ESDU 85020) and the integral length scales were set as 35m to 120m (figure 3a, ESDU 85020). Mean wind speed was set in the range of 6m/s to 20 m/s (based on flare stack design) for two extreme conditions (Bellasio (2012)).
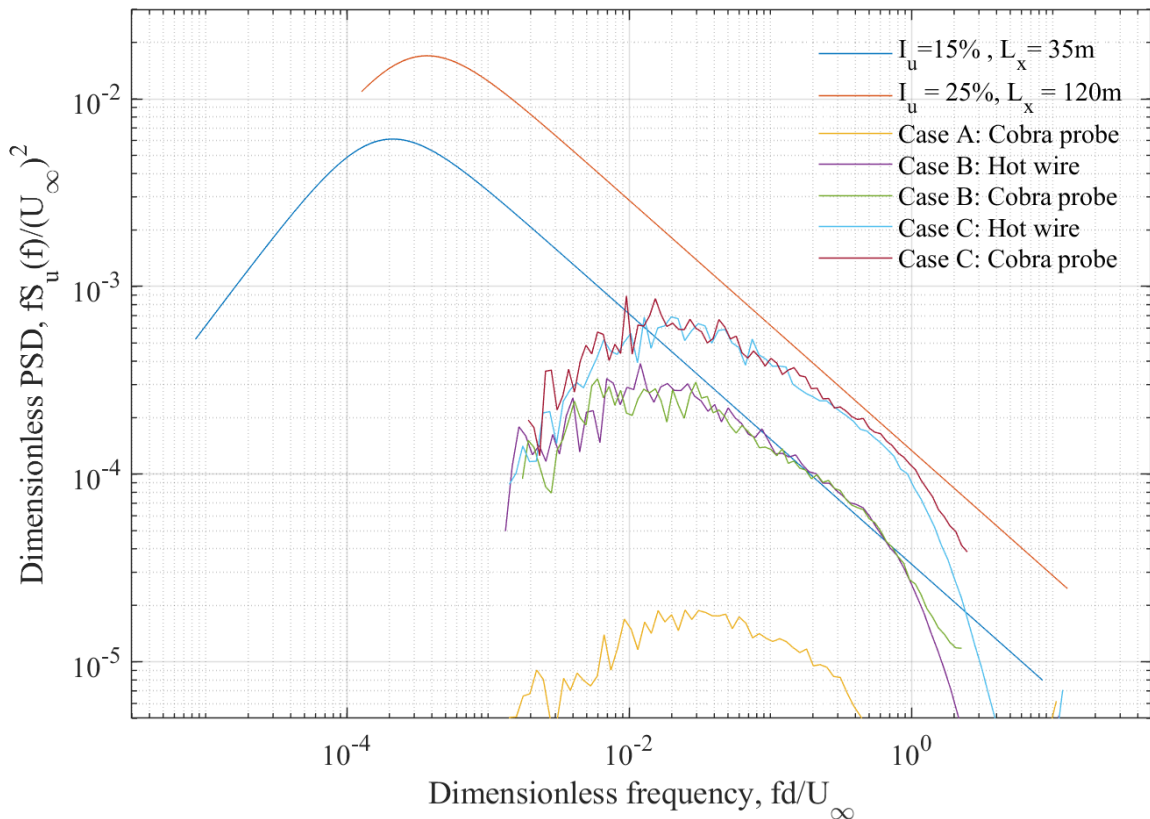
Figure 2.10: A graphical representation of real world turbulence to BLWT simulation in the form of dimensionless Power Spectral Density (PSD) vs dimensionless frequency. (Full scale Data is based on ESDU 85020).

Fig. 2.10 represents a comparison of these full scale scenarios to the experimental conditions of the wind tunnel where the dimensionless power spectral density (PSD) is plotted against dimensionless frequency. In the figure, the power spectral density is normalized using the local mean velocity, U_∞, so that differences in turbulence intensities are included in the plots, while stack diameter (d) is used to normalize the wave number (U_∞/f). Atmospheric scale turbulence has a large range of length scales and contains relatively a high level of energy. Meanwhile, the current wind tunnel induced turbulence has less energy at the large scales (low f) and, therefore, a lower overall energy level. In addition, the wind tunnel energy levels fall off rapidly for non-dimensional scales smaller than the jet diameter (fd/U_∞ ~ 1).

I_u < 1% represents a (approximately laminar) smooth flow case in this study. In a large boundary layer wind tunnel, turbulence intensity < 0.1% is very hard to obtain, but the spectrum indicates significantly reduced energy levels at all scales compared to the anticipated full scale values.

Chapter 3

3   Effect of flame length in crossflow

The classification of flames is provided, based on Huang and Chang (1999) in section 3.1 for methane rich fuel. An empirical relation for flame length is given based on Majeski(2000)'s model of natural gas, in section 3.2. The response of flame length to turbulent cross-wind is observed under the same section. A brief explanation of trajectory scaling is described in section 3.3. Section 3.4 provides a summary of the results presented in the chapter.

3.1   Classification of flames

To describe the flame from the instantaneous images, the whole set of flare experiments are divided into 3 main flow fields based on the momentum flux ratio.

1. Crossflow-dominated flame: $J \leq 0.66$
2. Transitional flame: $0.66 < J < 2.63$
3. Jet-dominated flame: $J \geq 2.63$

Huang and Wang (1999) additionally classified downwash flame. Downwash flame is discussed under crossflow-dominated flames. The Huang and Chang (1994), Huang and Wang (1999), Majeski et al.(2004) classifications distinguish the flame into different momentum ratios, as they use propane rich fuel. The general classification is briefly described in this section which assist to explain later parts of this chapter. In this section, the classification is based on smooth upstream flow (Iu < 1%).

3.1.1 Crossflow-dominated flames:

Figure 3.1 shows the instantaneous images of flame from camera 1 at very low momentum flux ratio J = 0.07 (U_∞ = 6 m/s, U_j = 2m/s). The X and Y-axis is non-dimensionalized by the burner inside diameter d = 26.64 mm. The stack effects the jet flame because of strong negative pressure on the leeward side. As the cross flow velocity is high compared to the jet velocity, the suction ($-P_{wake}$) generated on the leeward side is high and draws gaseous
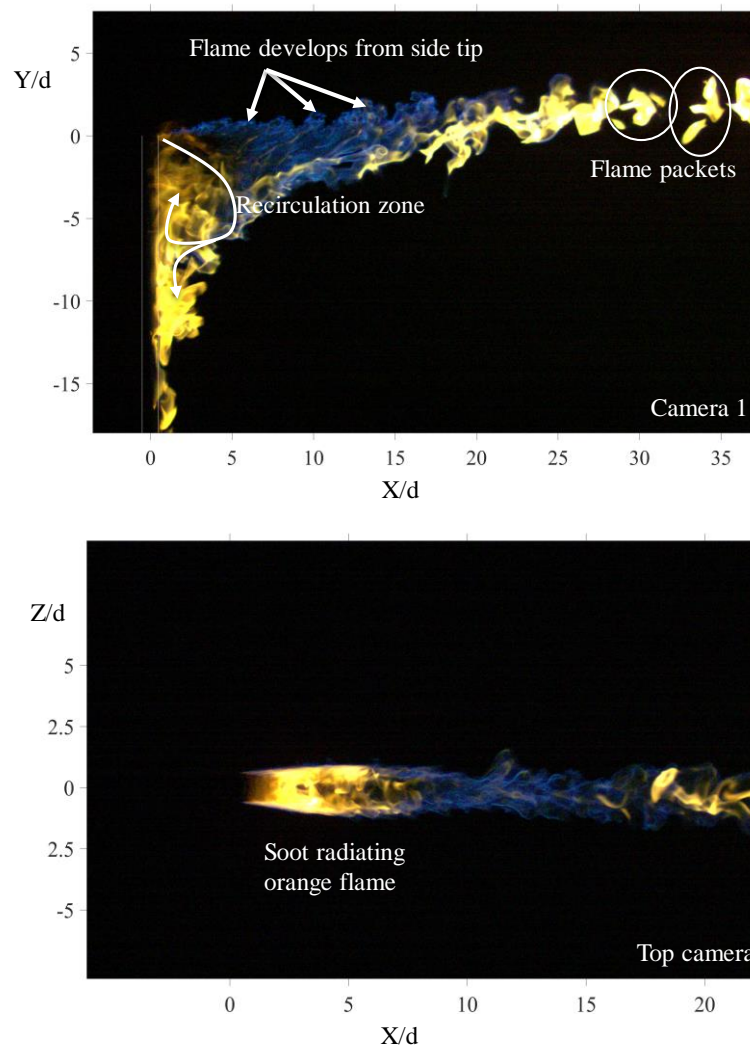
Figure 3.1: Instantaneous images of crossflow-dominated flame (U_∞ = 6 m/s, U_j = 2m/s , J = 0.07).

fuel in the downwash area. The difference in pressure between the free stream and the wake region behind the wall increases proportionally to the square of U_∞, but will also exhibit some Reynolds number dependence. Thus, the jet fuel emerging from the burner begins to show up on the leeward side of the stack. This is influenced by the crossflow, which bends the jet towards the right at a large angle. A wavy structure appears on the leeward side of the burner stack near the exit. This wavy structure evolves, grows, develops subsequently into small 'blobs' further downstream.
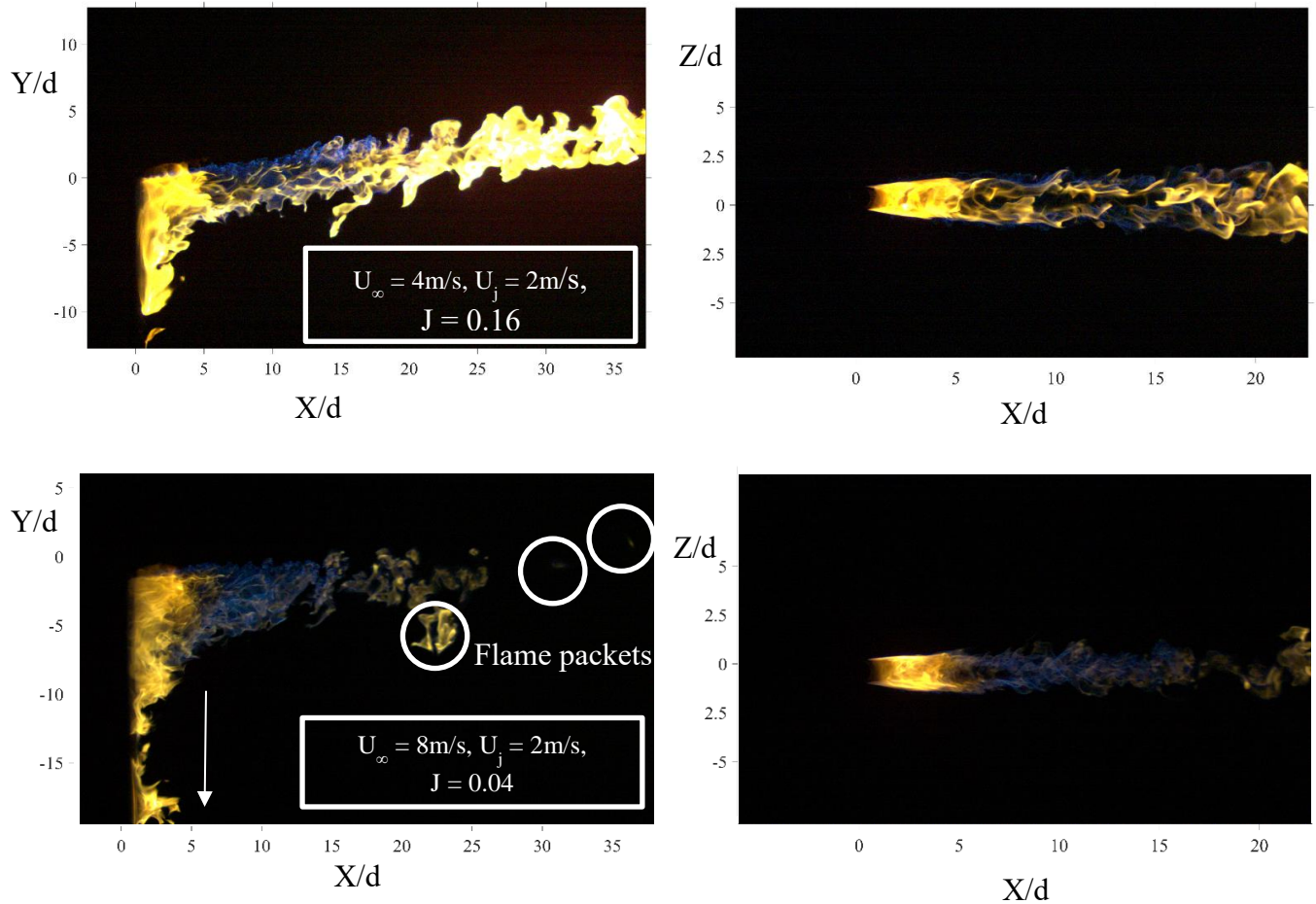
Figure 3.2: Instantaneous image of crossflow-dominated flame. Image on the right side indicates the corresponding field of view from top.

Momentum ratio less than 0.66 is termed as crossflow-dominated flame as the jet momentum is not large enough to sustain the impingement of the transverse stream. Fig. 3.2 represents instantaneous images attached for momentum ratio 0.04 and 0.16. As the momentum ratio is increased the recirculation zone decreases. A reduction of discrete flame packets and a decrease of downwash length is visible.

3.1.2 Transitional Flame

In the transitional flame, the downwash area reduces dramatically which is shown in fig. 3.3 for J = 0.66. A larger portion of gaseous fuel propagates downstream than the crossflow-dominated flame. A shear layer generates as a result of two fluid streams meet at an interface with a velocity difference. The shear layer seems to evolve from the side and spreads on lateral direction (fig. 3.3). A relatively small orange flame appears at the leeward side of the stack. Flame evolves from the burner stack showing a necking effect on the leeward side. The necking point seems like a source for the flow field. Necking effect is considered an essential feature for transitional flame (Huang and Wang, 2002).
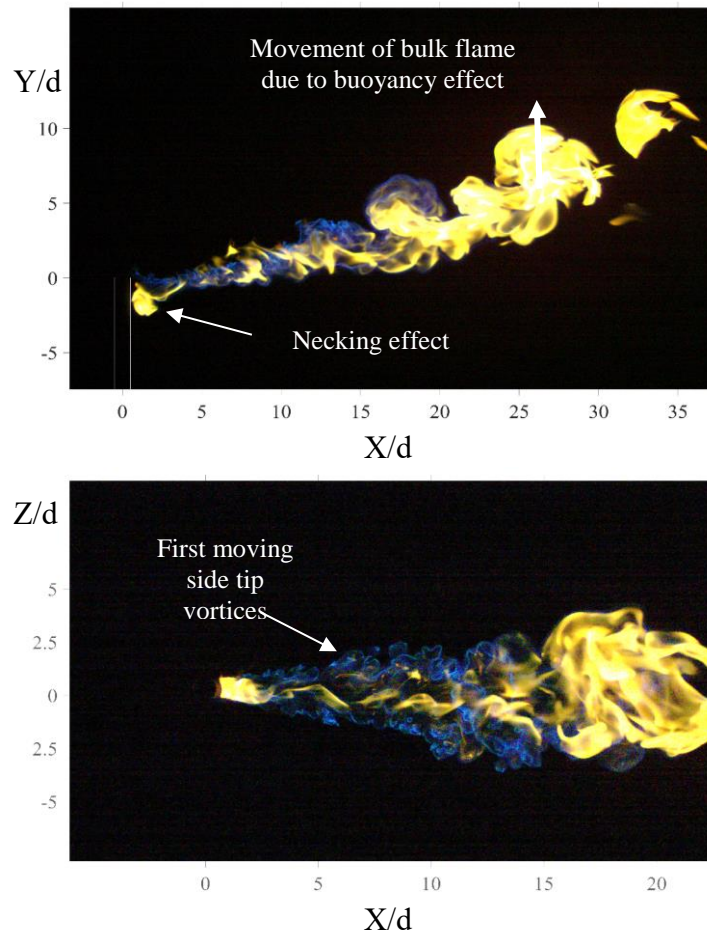
Figure 3.3: Instantaneous images of transitional flame (U$_\infty$ =2m/s, U$_j$ = 2m/s, J=0.66).

Comparing to crossflow-dominated flame, in transitional flame, the vortices in the shear layer still roll forward and are stretched in the x-direction. The shear layer vortices appear in a random fashion, stretching the flame in Z-direction enables air to fuel better mixing of fuel with air.

3.1.3 Jet-dominated flame

Figure 3.4 provides a depiction of jet-dominated flame. The initial deflection angle and the down-wash area for jet-dominated flame are comparatively small. At momentum ratio, J = 2.63, the mixing layer evolves from the windward side of the stack and trace of flame appears at leeward side of the stack (fig. 3.4). It is evident from the top image that vortices evolve from side is superimposed by crossflow and jet-flow Shear layer random nature suggest a strong turbulent mixing of the fuel and air. From the side image, there is no evidence of bending or necking effect like crossflow-dominated and transitional flame.
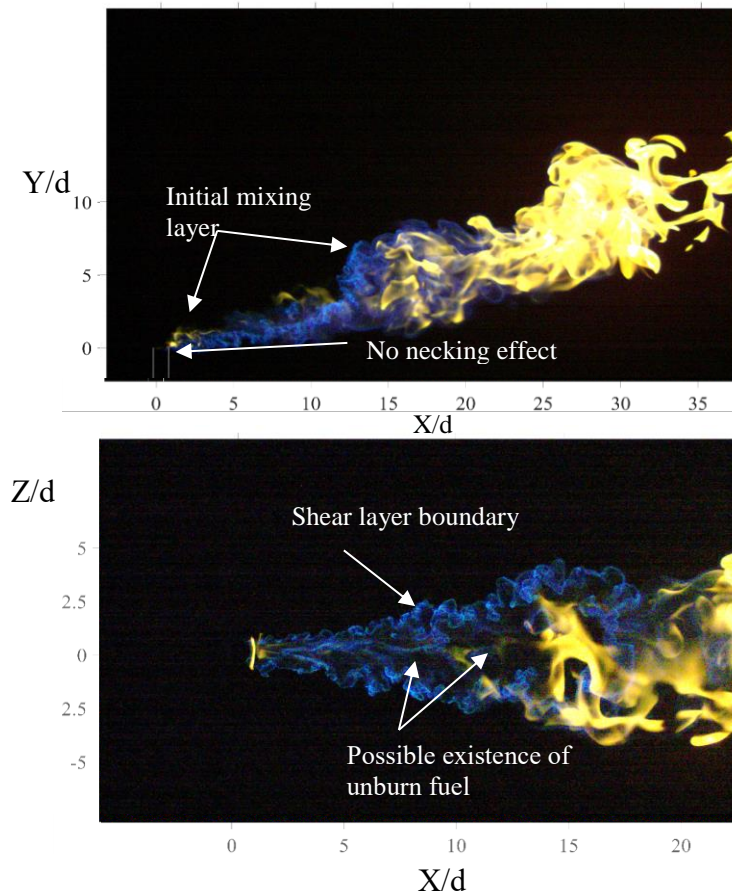
Figure 3.4: Instantaneous images of jet-dominated flame

(U_∞ = 4m/s, U_j = 2m/s, J=2.63)

The outer flame boundary (up to x/d < 15 in jet-dominated flame is more connected, wider but not symmetric in nature. However, the flame stabilizes in between the shear layer boundary. It is possible that heated unburned fuel exists in between the shear layer and starts burning in the orange radiated flame.
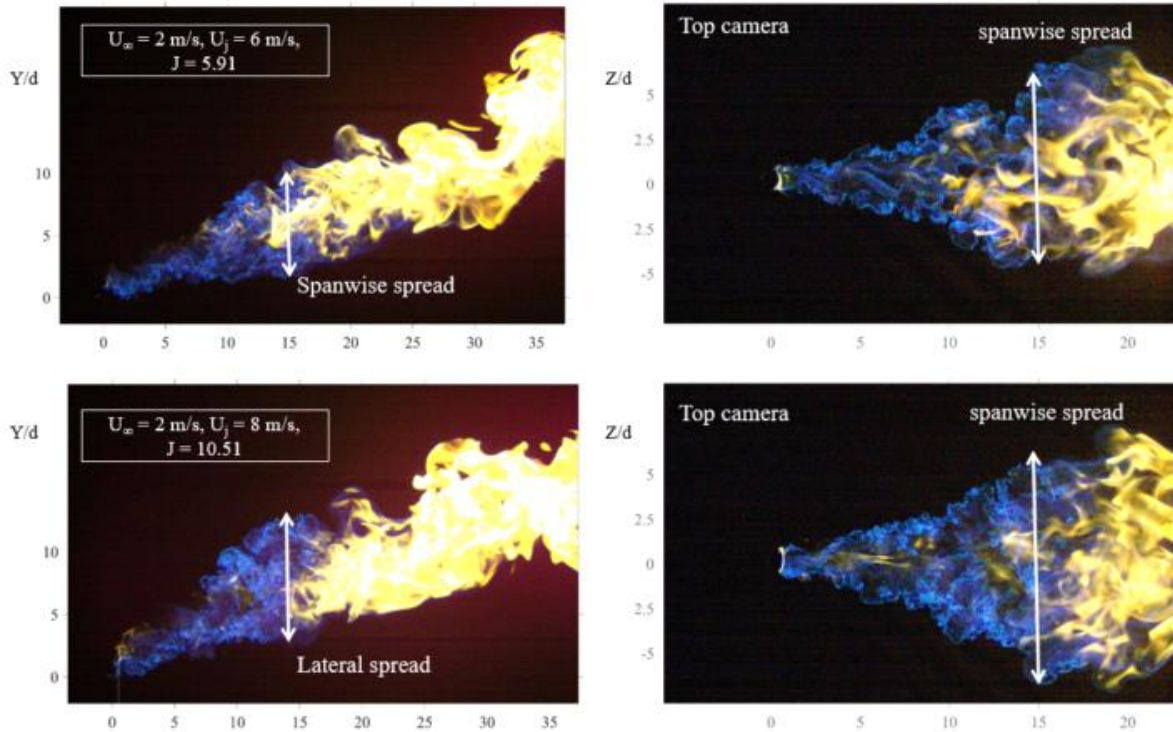
**Figure 3.5: Instantaneous image of jet-dominated flame at
different momentum ratios.**

The existence and size of the initial blue zone and the size is apparently a function of the intensity of fuel to air mixing process (Gollahalli el al.,1975). For jet-dominated flame, the mixing is higher than transitional or crossflow-dominated flame. The apparent reason is that the jet momentum is comparatively higher and therefore able to penetrate the crossflow. Additionally, the jet momentum can overcome the negative pressure impact behind the stack. The vertical and lateral spread of mixing layer expands with the increase

of momentum ratio (i.e. increase of jet velocity) which is visible from instantaneous images respectively from side and top cameras (fig. 3.5).

3.2   Flame Length

Flame length is defined as the linear distance between the flame tip and the centerline of the stack exit at the 10% occurrence of flame from average image (fig. 3.6). Image binarization for individual cameras and incorporation of 3 sets of images for a single set of experiments is explained in Appendix A.
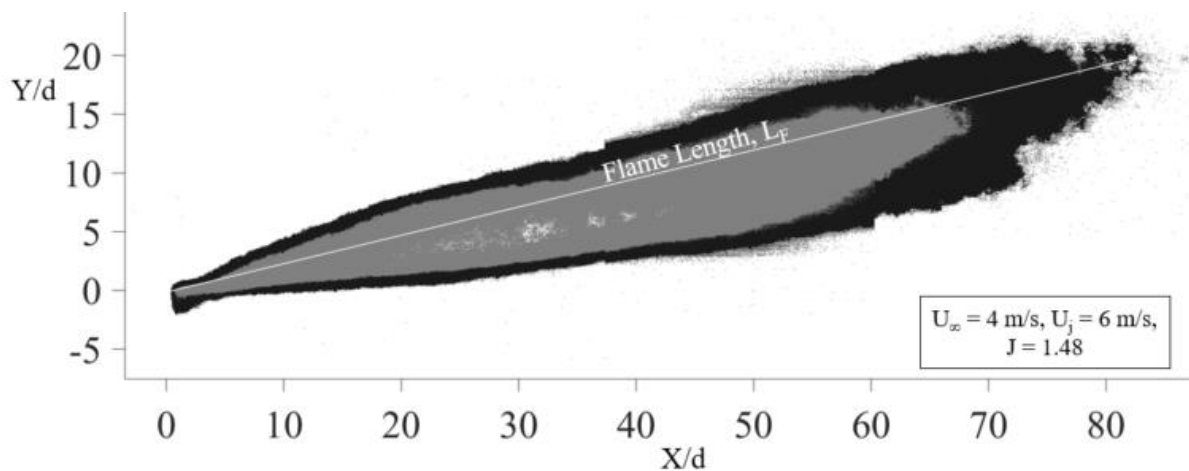
Figure 3.6: Mean full flame at J = 0.66 .

Majeski et al. (2004) gave an empirical model to determine the flame length for propane rich fuel over the range $5.9 * 10^{-3} < J < 4.6$. Majeski's model assumed that for any given set of fuel jet and crossflow properties the flame surface shape is geometrically similar. Additionally, the size of the flame was set by the time required for the stoichiometric amount of oxygen (O_2) to diffuse into and react with the fuel jet. On this point, the model can be extended to provide an empirical relation for predicting visible flame length (L_F) for methane flame as it exhibits similar physical phenomena as propane flame. For the

current study, the momentum ratio ranges from $3*10^{-2}$ to 10.51 and the diameter varies from 26.64 mm to 79 mm.

To accept Majeski's flame length model, the following equation for flame length must be compared with experimental data:

$$\frac{L_F}{C_f^{1/2} * U_\infty} = K_f (\rho_j U_j)^{1/2} \frac{d}{U_\infty} + K_U \qquad\qquad 3.1$$

where,

L_F = visible mean flame length; m,

C_f = concentration of fuel on jet = 0.978

K_f = flame constant, which is a combination of stoichiometric constant, geometric constant and the rate of oxygen arrival at the flame surface; $m*s^{1/2}/kg^{1/2}$,

K_u = constant of proportionality, which appears from the second assumption of Majeski's model; sec,

K_f and K_u are model coefficients that are important for determining the flame length empirically. The value changes with the change of fuel type. In order to determine model coefficients, equation eqn. 3.1 can be considered as follows:

$$Y_F = K_f * X_F + K_u \qquad\qquad 3.2$$

where, X_F, Y_F are Cartesian variables. K_f is the slope and K_u is the Y-intercept in fig. 3.7**.** The data collapse into two different region, providing support for the modeling assumptions of geometrically similar flame shape and diffusion-limited combustion for methane flame.
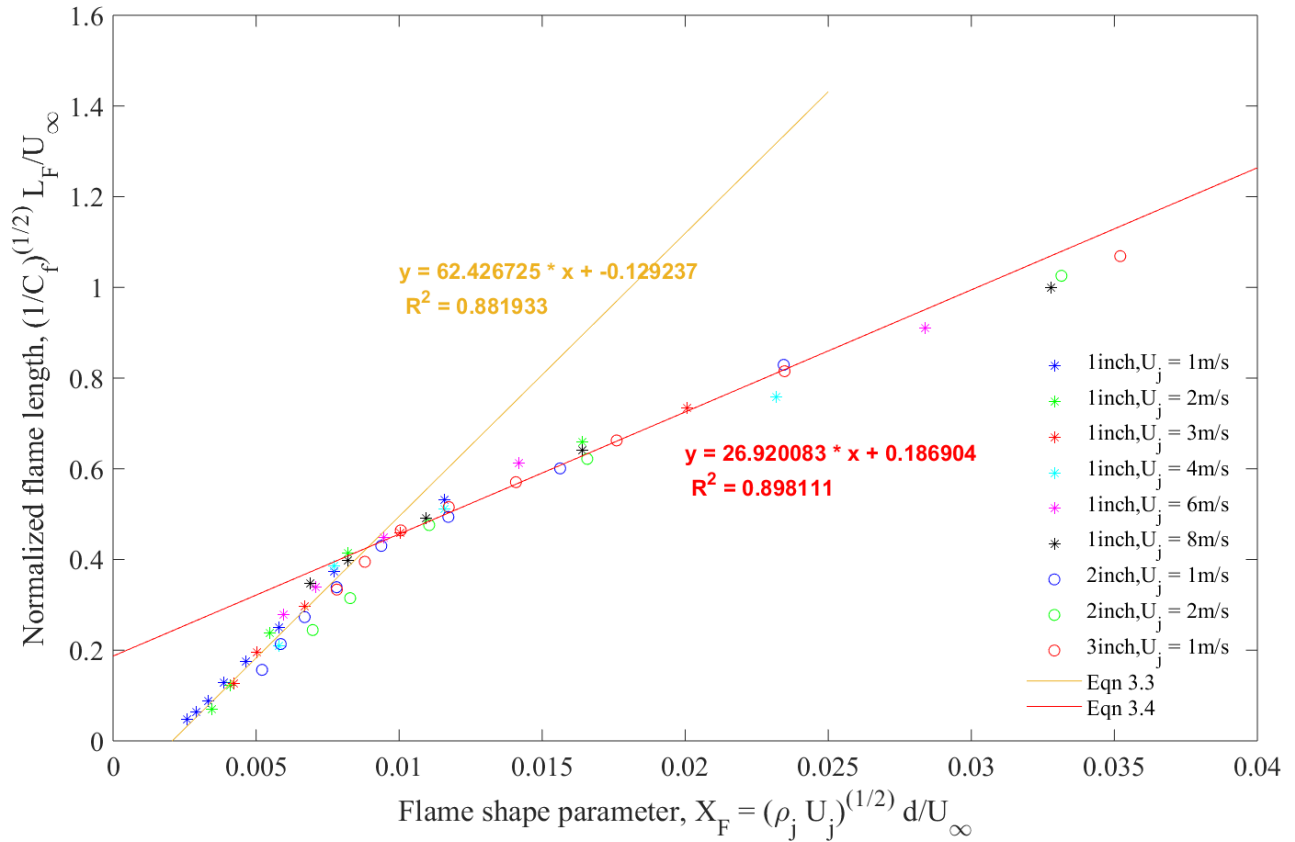
Figure 3.7: Flame length data plotted with respect to the variables described eqn. 3.2.

The plotted data renders a slope change at $X_F = 7.7*10^{-3}$. The slope change point is considered as discontinuity point. After that discontinuity point, L_F increases with increasing U_∞(eqn. 3.4) and before that discontinuity point, L_F shortens with increasing $U\infty$(eqn. 3.3). The best fit lines with the intersection were found by minimizing the root mean square(RMS) error with respect to normalized flame length. This procedure is quite consistent with Majeski's(2004) approach. For Methane rich flame, the resulting functions are:

$$\frac{L_F}{C_f^{1/2} * U_\infty} = 62.427 * (\rho_j U_j)^{1/2} \frac{d}{U_\infty} - 0.129 \qquad 3.3$$

$$\frac{L_F}{C_f^{1/2} * U_\infty} = 26.920 * \left(\rho_j U_j\right)^{1/2} \frac{d}{U_\infty} + 0.187 \qquad\qquad 3.4$$

The lines for propane flame (Majeski el al., 2004) agreed with the data within an RMS error of 15% whereas, the RMS error of the current study is less than 11%. The uncertainty of the current analysis is discussed later on Appendix B.

The model equation is plotted with the actual data in dimensional form to understand in a better way. Flame length(L_F) vs crossflow velocity(U_∞) is plotted in fig. 3.8. The general trend is that flame length is increasing with crossflow velocity for jet-dominated flame and transitional flames. But the flame length decreases with increasing crossflow velocity for strong crossflow-dominated flames. The empirical relations for both regimes offers a good
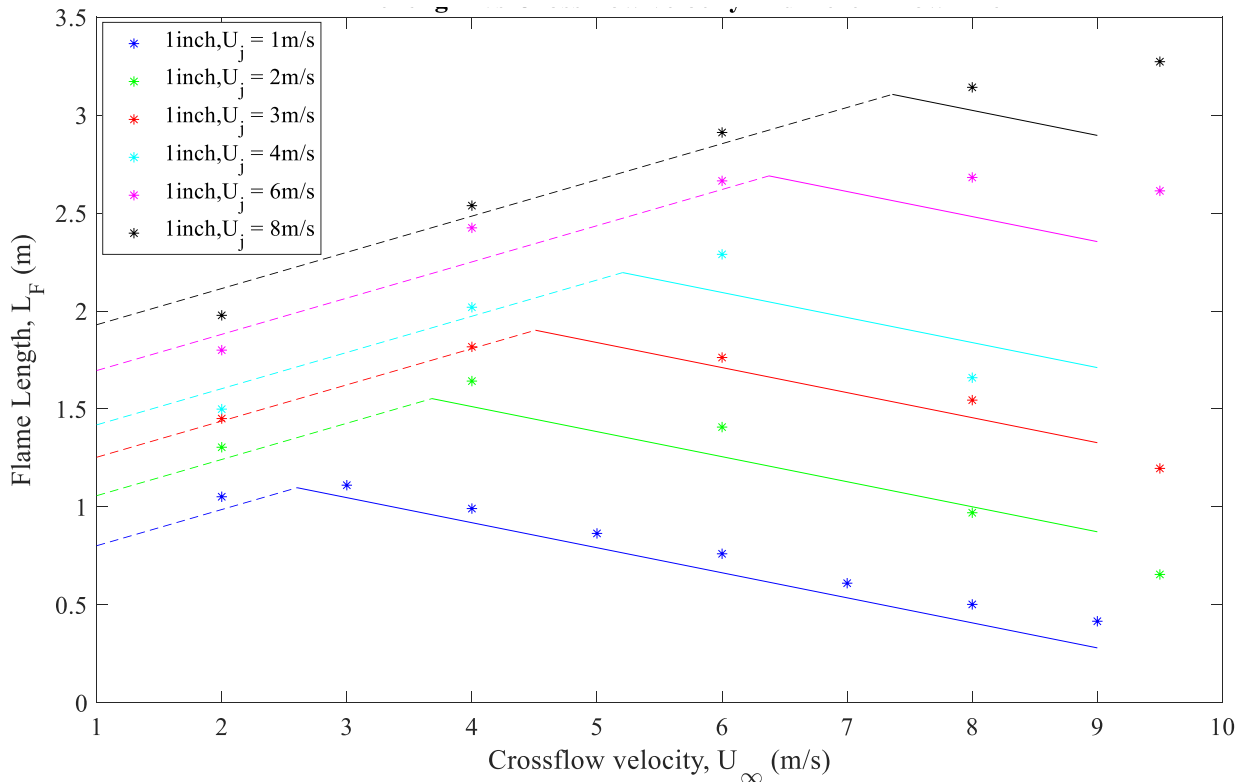
Figure 3.8: The jet exit velocity (Uj) scaling data for combusting gas compared with the empirical equation. Solid line represents eqn. 3.3 and dotted line represents eqn. 3.4.

agreement with experimental data for a wide range of jet velocities(fig. 3.8) and for different diameters (fig. 3.9). The overall RMS error for fig. 3.8 and fig. 3.9 are 23% and 21% respectively.

The model equation predict flame length well for low to moderate jet velocity ($U_j < 6$ m/s) and for different stack diameter with good agreement. However, at high jet velocity ($U_j \geq 6$), the empirical equation underpredicts the flame length(L_F) at high crossflow velocity(fig. 3.8). Moreover, instead of being getting decreased at high crossflow velocity, the flame length follows the increasing trend.
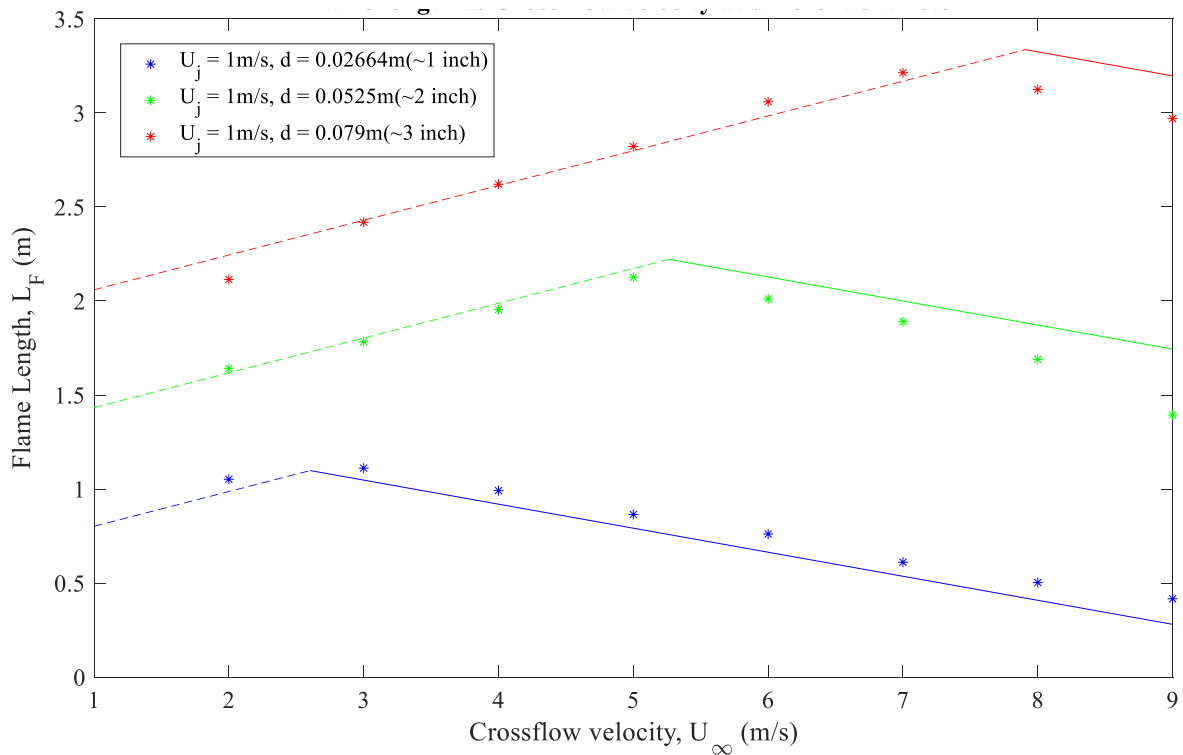
Figure 3.9: The stack diameter (d) scaling data for combusting gas compared with the empirical equation. Solid line represents eqn. 3.3 and dotted line represents eqn. 3.4.

Majeski el al.(2004) estimate a 13% error for different diameter burner (21% in the present case). Majeski et al. (2004) used a 33 mm inner diameter flare stack was used as max diameter for the propane flame length modeling. Meanwhile, for the current experiment,

77 mm inner diameter burner is used as max diameter burner to predict flame length for industrial case.

3.2.1 Effect of turbulent cross-wind on flame length

The flame length responds to turbulent crossflow. However, the changes are not quite significant. For transitional and jet-dominated flames, the flame length for smooth crossflow ($I_u<1\%$) is higher than turbulent crossflow (fig. 3.10). The decrease in flame length due to higher turbulent crossflow is generally within 8-10% within the smooth flow flame length. The trend is generally consistent for different flow conditions. The decrease in flame length for turbulent cross-wind is likely for the spread of flames in the lateral and vertical direction. The mean spread of the flames will be discussed in the next chapter.
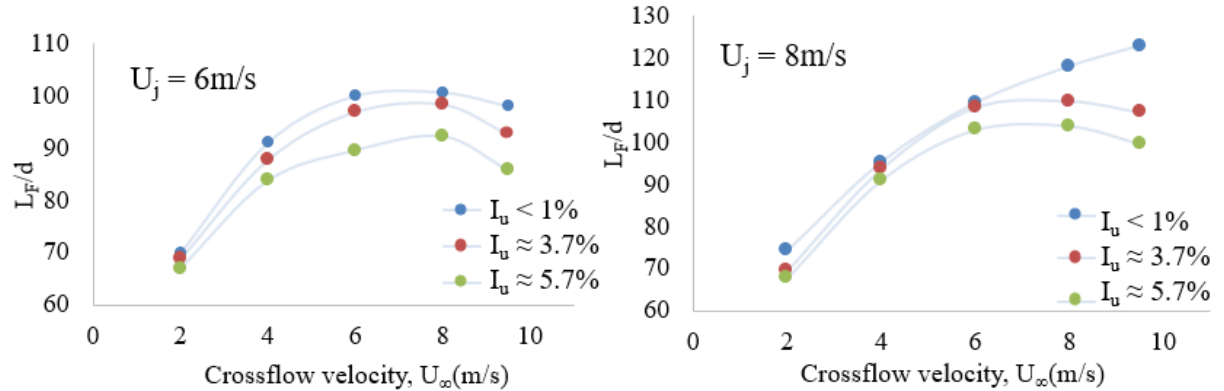
Figure 3.10: Dimensionless flame length vs cross flow velocity at jet velocity 6m/s(left) and 8m/s(right). (Burner diameter: 2.664cm).

The trend of shorter flame length at high turbulent cases altered when crossflow momentum is very strong. At higher turbulence case ($I_u \approx 3.7$ and $I_u \approx 5.7$) the flame length is slightly higher than the smooth flow case ($I_u < 1\%$). Figure 3.11 illustrates the effect at jet velocity 2 m/s and 4 m/s. At high crossflow velocity (8 m/s and 9.5 m/s) the flame length for smooth flow is shorter than turbulent flow (fig. 3.11, $U_j = 2$ m/s). A strong recirculation zone (for smooth flow condition) may play an important mechanism for this effect.
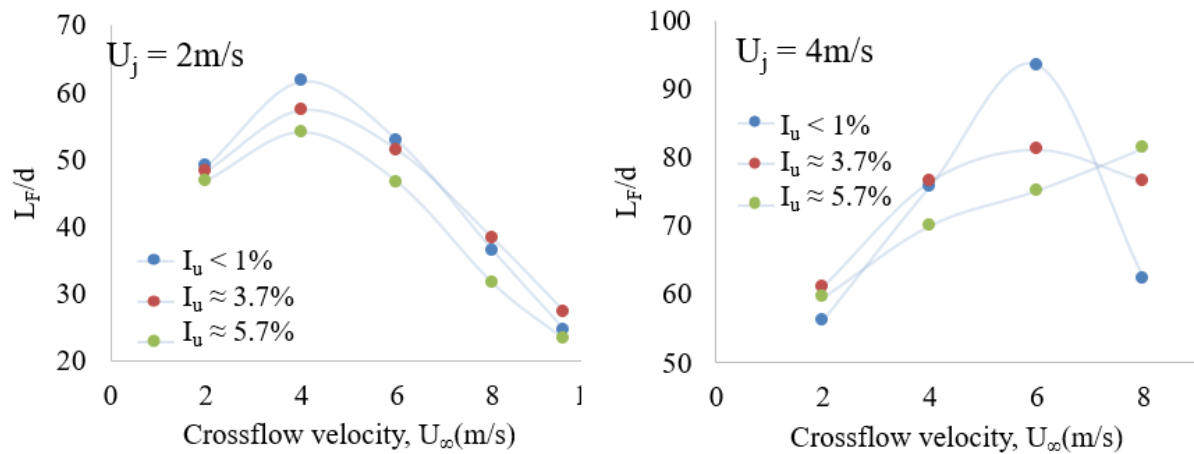
Figure 3.11: Dimensionless flame length vs cross flow velocity at jet velocity 2m/s(left) and 4m/s(right). (Burner diameter: 2.664cm).

3.3 Flame Trajectory

Smith and Mungal(1998) define trajectory as the maximum concentration line. Katamoni and Greber (1972) define the jet trajectory using the velocity maxima. Mupiddi and Mahesh (2005) define jet the trajectory based on the mean streamline. Ryan et al. (2014) define jet trajectory from flame luminosity. In this study, flame trajectory are defined from mean flame images. Midpoint of 10 % contour along vertical direction is defined as flame trajectory. Flame trajectory can also be defined as jet centerline in this study.

Figure 3.12 represents a comparison of flame trajectory at different scaling method. The flame jet trajectory is normalized by velocity ratio(r) times diameter (left), and momentum ratio (J) times diameter (right). Three different velocity pairs are considered and the crossflow is smooth ($I_u < 1\%$). It is observed that trajectories collapsed comparatively better while 'Jd' scaling is used. Trajectories do not collapse well with 'rd' scaling, which is previously observed for cold flow trajectories (Pratte and Baines, 1963; Smith and Mungal, 1998).
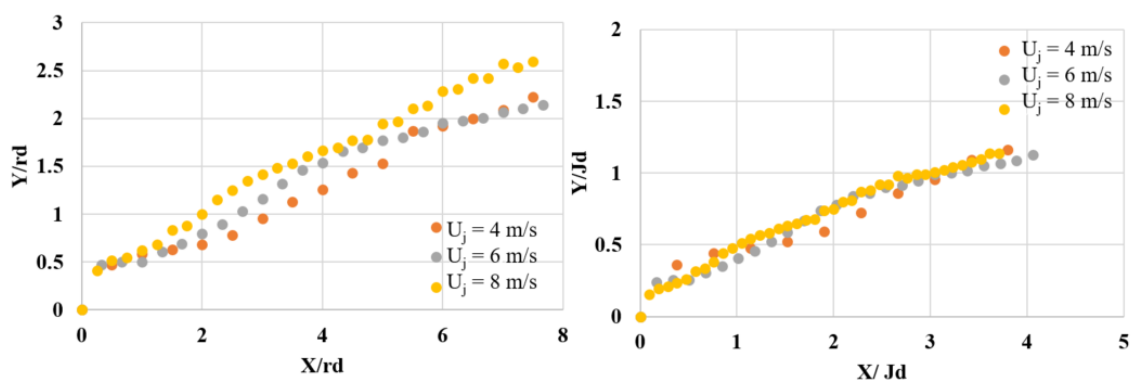
Figure 3.12: Comparison of jet trajectory in different scaling method ($U_\infty = 2m/s$).

3.4 Summary

The main focus of this chapter is to develop co-efficient of Majeski's model and verify the empirical relations to experimental results of flame length. The response of flame length to turbulent crossflow is observed. The image analysis procedure and uncertainty analysis are included in the Appendix A and Appendix B. The main findings of this chapter are:

- Classification of the flame is given based on Huang and Chang (1994) and Huang and Wang (1999) and Majeski et al. (2004). However, the previous model is based on propane rich fuel. The physical phenomenon of the deflected flame happens on different momentum ratios for methane-rich flame for the current study. Empirical equations are provided based on experimental values of flame length.

- The overall RMS error of the empirical and experimental values is less than 23%. The current experiments have been conducted for a wide range of momentum flux ratios, higher jet velocity, and larger stack diameter compare to previous model. These are the reasons for higher RMS error.

- The empirical equation slightly underpredicts the flame length at low jet velocity and overpredicts at high jet velocity. The flame length cannot be predicted accurately when there is strong downwash flame. As a result of strong downwash, the flame does not look like a cylinder which is a violation of the first assumption of the existing model. Those reasons may result in lower accuracy for the current empirical equation for methane flame.

- Flame length reduces (8-10%) as a result of enhanced turbulent crossflow (fig. 3.10). However, at very strong crossflow (when the downwash region is very large) the flame length is shorter for smooth flow condition (fig. 3.11).

- Flame trajectories collapse to a single path when normalized by momentum flux ratio (fig. 3.12).

Chapter 4

4   Effect of crossflow turbulence on flames

In this chapter, the results of the effects of the turbulent crossflow are presented. There are 3 experimental cases discussed, namely, case A ($I_u < 1\%$), case B ($I_u \approx 3.7\%$, $L_x = 0.23$m) and case C ($I_u \approx 5.7\%$, $L_x = 0.32$m) in chapter 2. In chapter 3, effect of turbulence on flame length were discussed. In this chapter, the effect of turbulence cross-wind will be discussed based on instantaneous and mean flame images. In section 4.1 an analysis of wake recirculation zone is carried on with the help of mean images. In addition, the spread of the flame both in the vertical and lateral directions due to crossflow are discussed under section 4.2. A comprehensive study of the discrete 'blobs' will be carried out using instantaneous images in section 4.3. In section 4.4 the colour of the flame is analyzed in order to distinguish the mixing phenomena of crossflow fluid and jet fluid in the near field. Image segmentation is employed to understand this more clearly.

4.1   Wake recirculation zone

The recirculation zone on the leeward side of the stack is a basic characteristic of crossflow-dominated and transitional flames (Section 3.1). In this section, mean flame images are utilized to distinguish different crossflow conditions. The methodology to obtain a mean flame image from instantaneous images is described in Appendix A.

Fig. 4.1 depicts the mean images of a crossflow-dominated flame ($U_\infty = 4$m/s, $U_j = 2$m/s) for different turbulence conditions. The size of the flame is non-dimensionalized by the size of the inner diameter of the stack. The size of the recirculation zone (marked on the figure) is smaller for a larger level of crossflow turbulence. These phenomena can be clearly visualized in an integrated mean flame image, such as that in fig. 4.2. The figure indicates that recirculation zone is largest for smooth flow case. This suggests that the recirculation zone draws more fuel in this flow condition (case A, $I_u < 1\%$). The result is consistent for the other crossflow-dominated flame. Fig. 4.3 represents integrated mean flame images from side cameras with $U_\infty = 6$m/s, $U_j = 4$m/s.
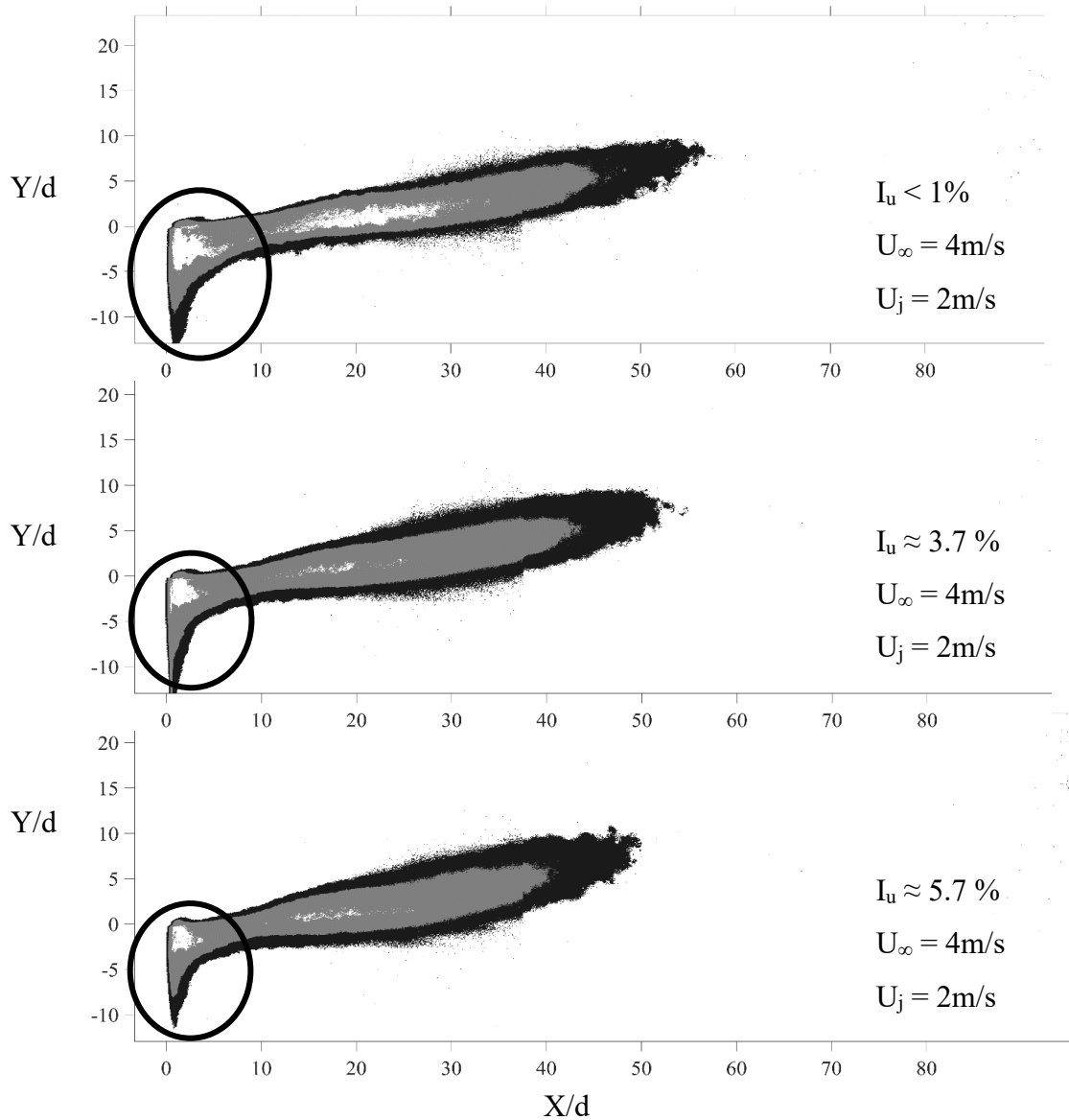
Figure 4.1 : Mean flame for three turbulent condition.

While no pressure measurement have been taken on the leeward side during this study, it may be worthwhile to assume that the pressure is comparatively lower on the leeward side for reduced turbulence intensity. Smooth crossflow is vulnerable to adverse pressure gradient on the rear of the cylinder (no jet flow), and separation occurs earlier than turbulent

condition (White, 2004). As a result, the pressure on the leeward side vertical wall of the stack is comparatively higher in turbulent crossflow. The suction of fuel in the leeward side recirculation zone is thus comparatively less for enhanced turbulence crossflow.
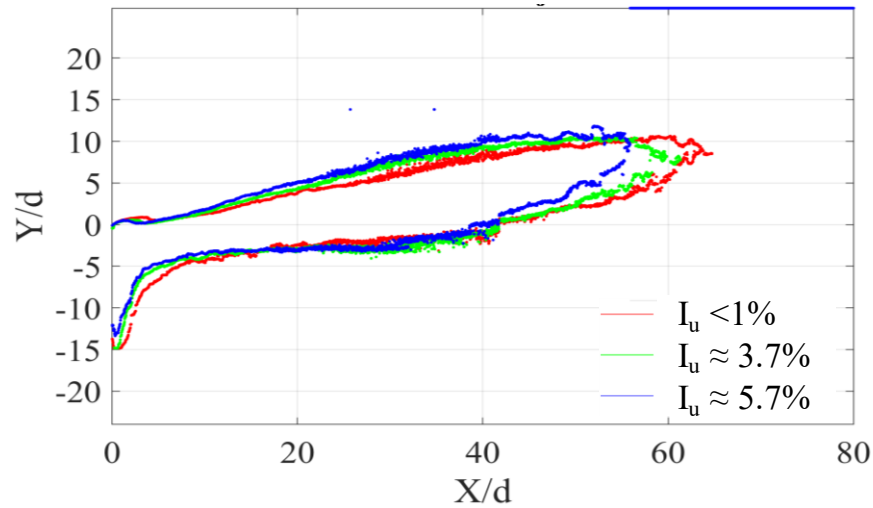
Figure 4.2: Integrated mean flame image for different turbulent conditions (U_∞ = 4m/s, U_j = 2m/s).
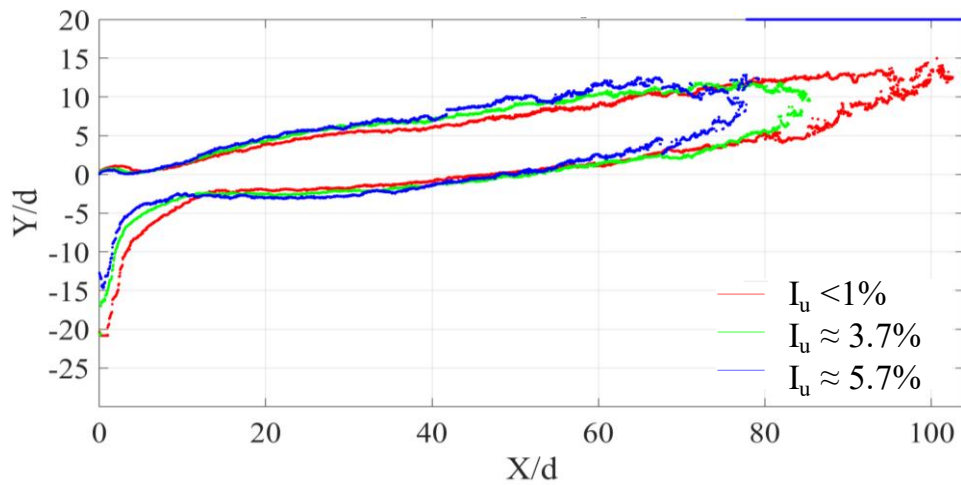
Figure 4.3: Integrated mean flame image for different turbulent conditions (U_∞ = 6m/s, U_j = 4m/s).

4.2   The spread of the flame

Figure 4.4 shows dimensionless spread of the flame in the vertical direction (ΔY/d) versus dimensionless downstream distance (X/d), obtained from photographs depicted in figure 4.1. Figure 4.4 contains an initial spreading region(X/d<4) due to the presence of a strong recirculation zone followed by a minima between X/d = 4 to 10, depending on the turbulence level. The mean flame continues to spread up to X/d = 30 and stabilizes up to X/d< 40. The expansion zone (10<X/d<40) indicates air-fuel mixing and combustion of pyrolyzed components of fuel (Gollahalli et al., 1975). A decrease in flame spread in size indicates a reduction in the rate of combustion after X/d >40.
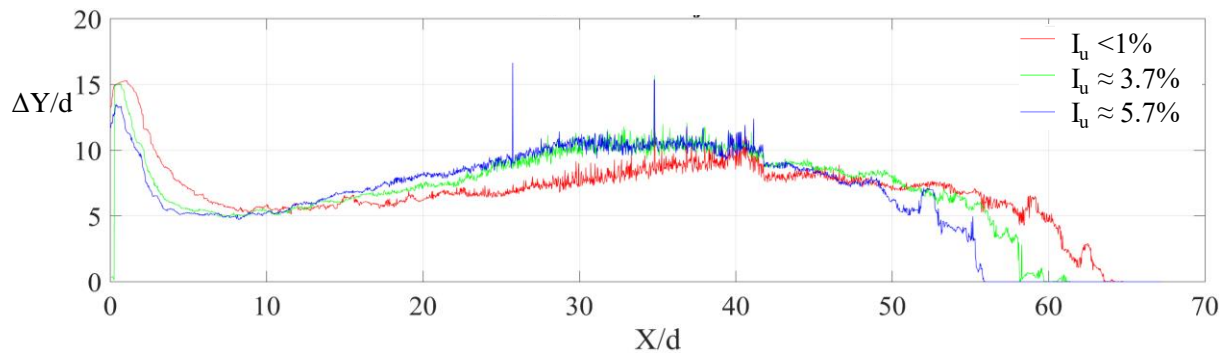
Figure 4.4: Mean spread of the flame for different turbulence conditions.

In fig. 4.4, the vertical spread of flame (10 < X/d < 40) happens slightly faster in the turbulent case. This indicates an enhanced rate of combustion of pyrolyzed components of fuel in that region for case B and case C. Following the rapid spread zone, the visible flame for enhanced turbulence shows an earlier extinction when compared to the smooth flow condition (case A, I_u <1%). This result is consistent at U_∞ = 6m/s, U_j = 4m/s (fig. 4.5a). Both fig. 4.4 and fig. 4.5 represent crossflow-dominated flames. In addition, the vertical spread of jet-dominated flame also shows a similar kind of trend (fig. 4.5(b,c)).

(a) $U_\infty = 6m/s$, $U_j = 4m/s$

(b) $U_\infty = 4m/s$, $U_j = 6m/s$

(c) $U_\infty = 4m/s$, $U_j = 8m/s$
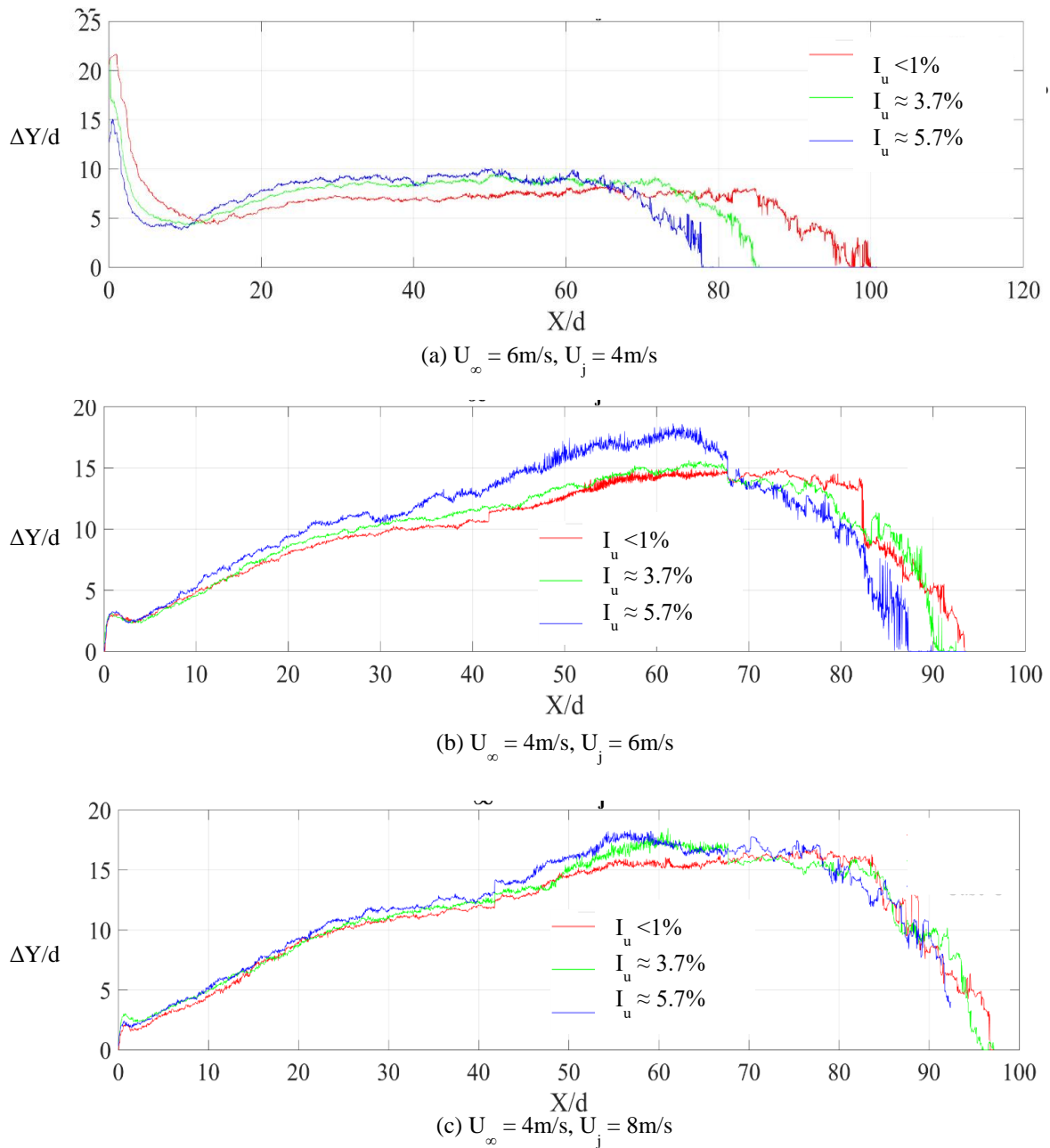
Figure 4.5: Vertical spread of the flame for different velocity magnitudes.

Fig. 4.6a provides the shape of the mean flame (outline of 10% contour) captured from the top camera for three different turbulent cases. Fig 4.6b represents the width of the dispersion in the lateral direction. No significant effect of flame spread in the lateral

direction is visible in the near field (X/d<10). The flame spreads rapidly after that X/d>10. The spread is faster for enhanced crossflow turbulence.
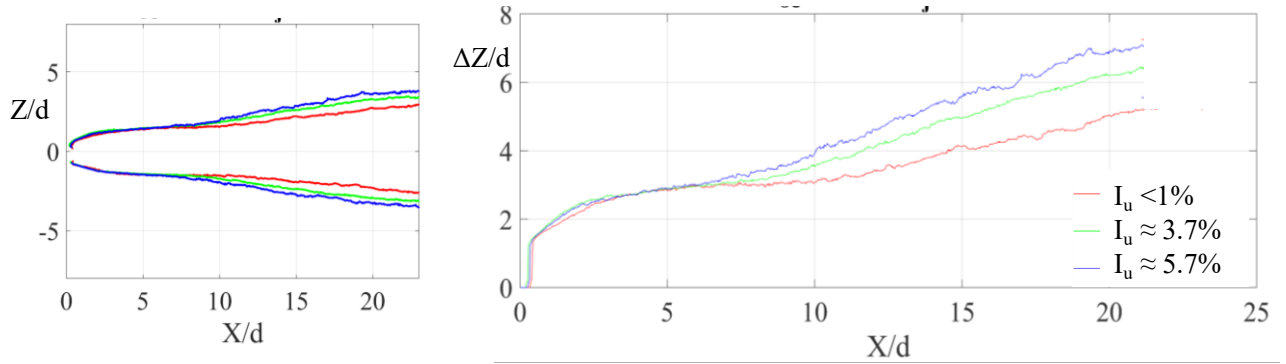
Figure 4.6: (a) Outline of 10% contour of mean flame for different turbulent conditions (image captured from top camera); (b) Lateral dispersion of the mean flame (U_∞ = 4m/s, U_j = 2m/s).

The result are consistent at U_∞ = 6m/s, U_j = 4m/s, which is represented in fig. 4.7a. Due to the nature of grid turbulence, a strong lateral (I_w) turbulence is induced, which is intended to increase of mean flame spread in the Z-axis in the far field.

Both fig. 4.6b and fig. 4.7a depict crossflow-dominated flames. However, for stronger jet momentum, there is no significant variation of the lateral dispersion for enhanced crossflow turbulence (fig. 4.7b,c). Thus it appears that the strong jet momentum may overwhelm the differences of the crossflow turbulence properties.
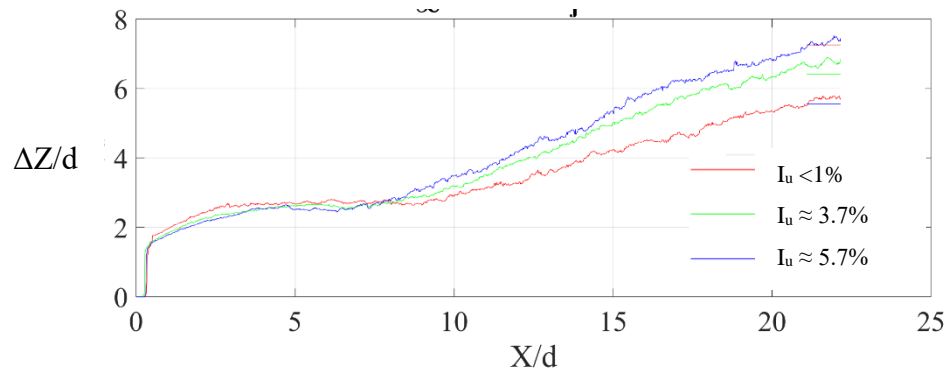
(a) $U_\infty = 6$m/s, $U_j = 4$m/s
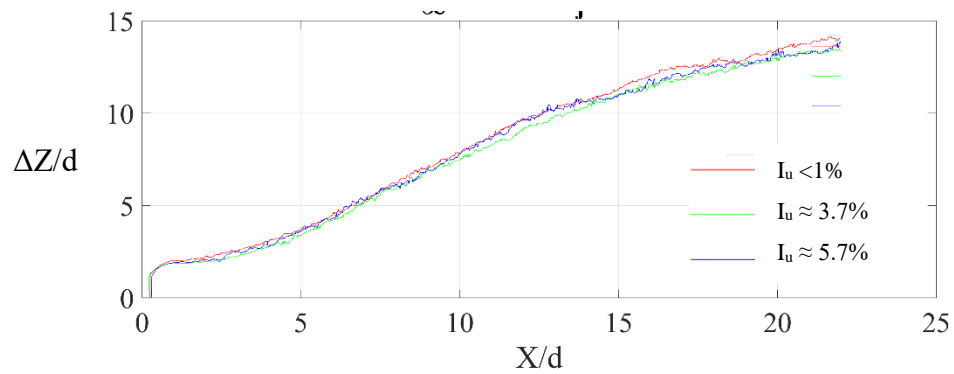
(b) $U_\infty = 2$m/s, $U_j = 6$m/s
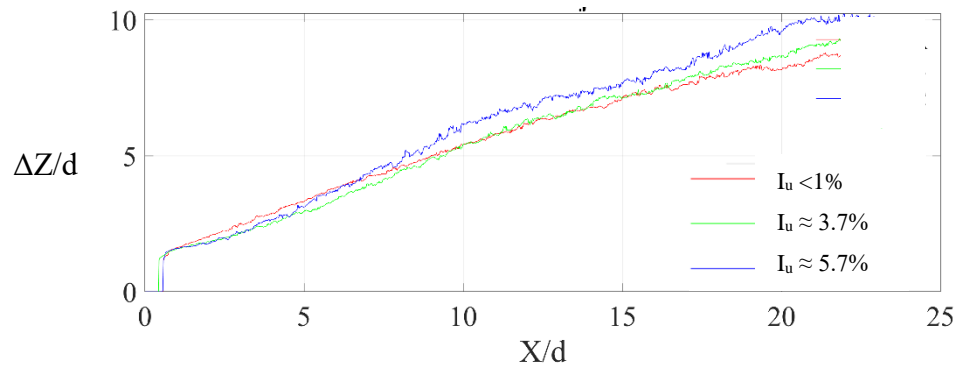
(c) $U_\infty = 4$m/s, $U_j = 6$m/s

Figure 4.7: Lateral spread of flames for different velocity magnitudes.

4.3 Analysis of the discrete flame packets

Discrete flame packets are an essential feature of crossflow-dominated flames. In fig. 4.8a, it is seen that as the crossflow velocity increases the upper flame surface wrinkles and later generates discrete flames packets. It is observed that the location where the flame starts to fragment is closer to the stack for large values of U_∞ (fig 3.2). Kostiuk el at.(2000) reported that discrete flame packets are responsible for reducing carbon combustion efficiency. In this section, it will be verified that if enhanced crossflow turbulence has an effect on the discrete flame packets.
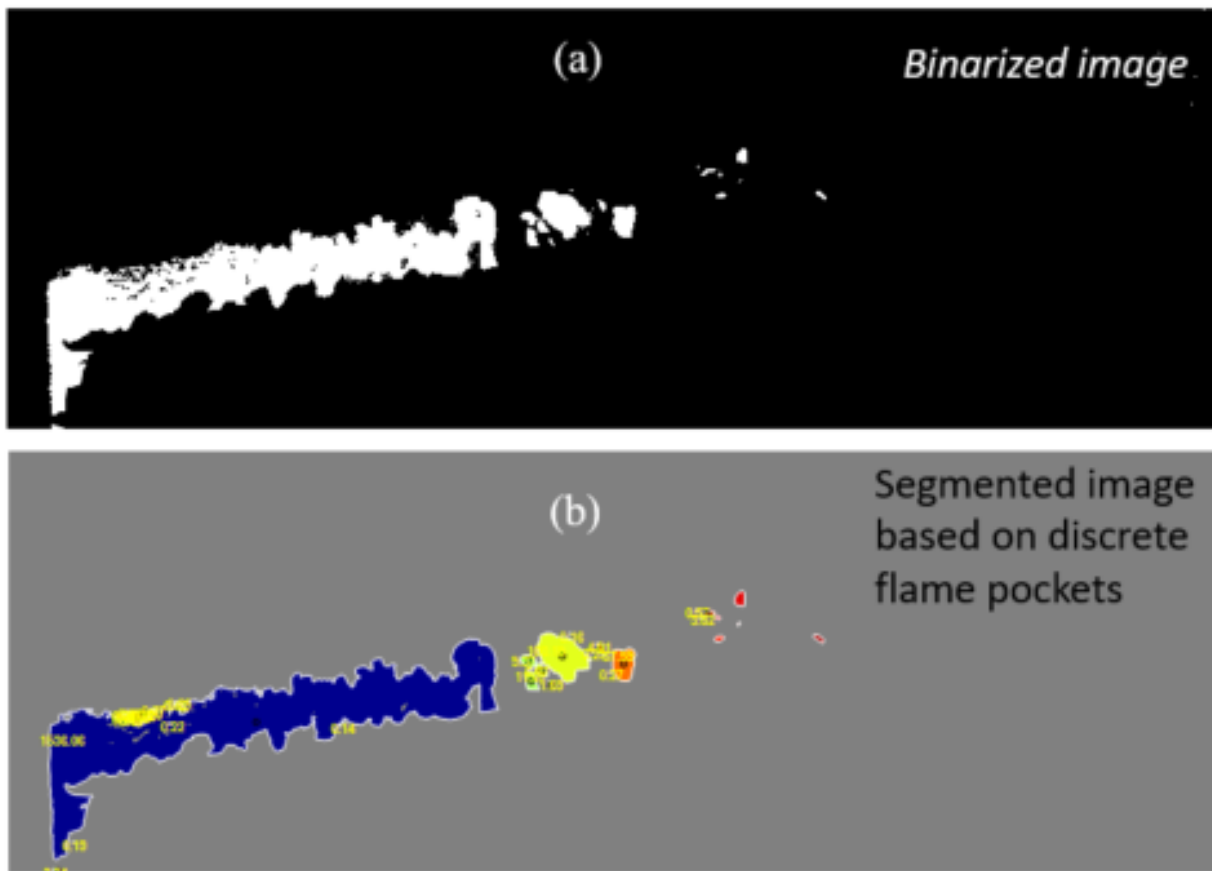
Figure 4.8: Analysis of discrete flame packets (U_∞ = 4m/s, U_j = 2m/s).

The image processing steps to get mean flame packet numbers are explained in Appendix A.3. Fig. 4.9 provides a comparison of discrete flame packet numbers for different

turbulence conditions. At $U_\infty = 4$m/s, there is an increased number of average flame packets for enhanced turbulence (case B, case C). However, the result is not consistent with other crossflow velocities (6m/s, 8m/s). It would be worthwhile to assume that stack wake shear layer vortices are mainly responsible for generating discrete flame packets (Majeski, 2000). From the current cases, it appears that turbulence has no significant effect on the number of discrete flame packets (blobs).
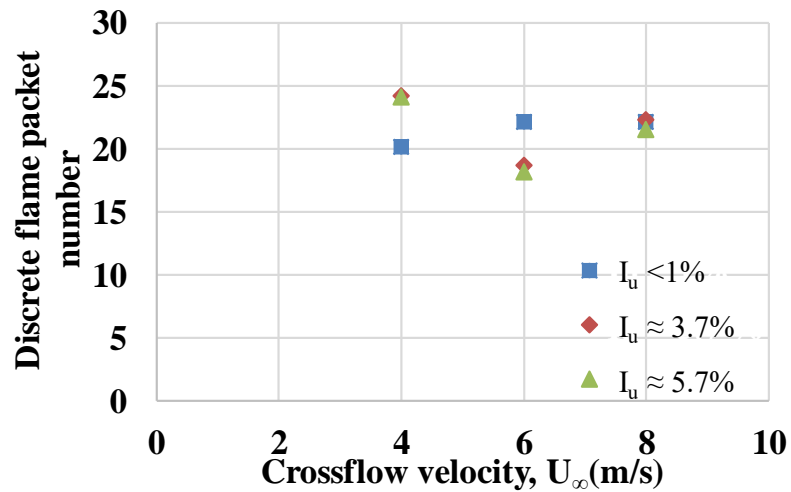
Figure 4.9: Relation between discrete blob no. to crossflow velocity at $U_j = 2$m/s.

It has been observed (not shown here) that detached flame packets also appear for jet-dominated flames. Such flames are detached from the main body on the tip side. Flame packets for different crossflow turbulence conditions do not vary consistently. However, turbulence does not appear to have a significant effect on discrete flame packets on jet-dominated flames as well.

4.4 Flame colour analysis

There is an intense mixing of the jet fluid and ambient air in the near field of the stack. This phenomenon results in blue flames which correspond to a premixed combustion behavior (Gollahalli et al., 1975). The yellow or orange flames are due to incandescence of very fine soot particles that are produced in the flame. In this study, the segmentation of images based on colour is explained in the Appendix A. Fig. 4.10 presents an instantaneous image captured from the top camera. The corresponding flow conditions are mentioned in the figure. The blue portions of the flame are observed to be narrower in the near field (0<X/d<5) for enhanced turbulent crossflow. Laminar crossflow is vulnerable to adverse pressure gradient on the rear of the cylinder (no jet flow), and separation occurs earlier than turbulent condition (White, 2004). This phenomenon may similar to narrower flame in the near field due to induced turbulence (Fig. 4.10). However, the flame overcomes the
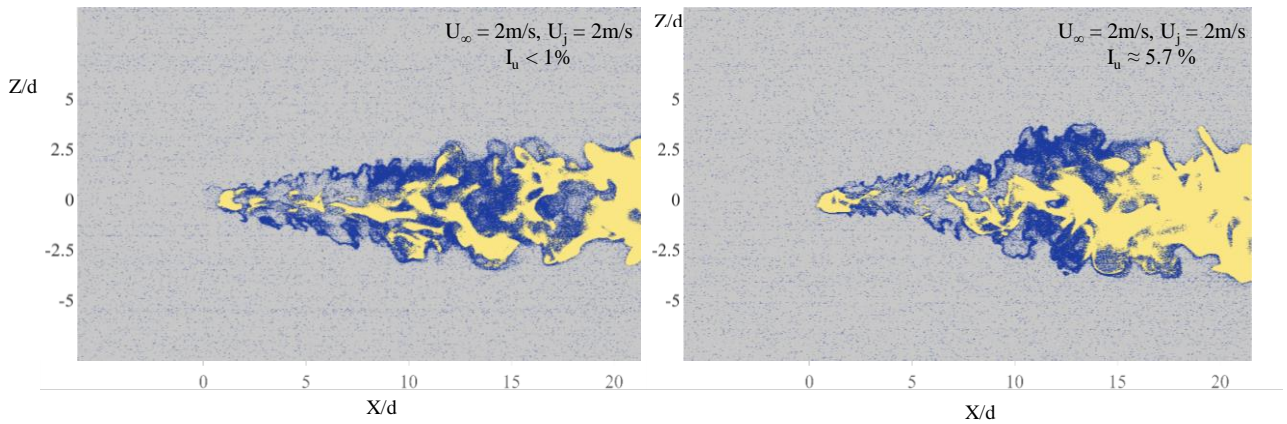
Figure 4.10: Analysis of instantaneous images at U_j = 2m/s and U_∞ = 2m/s for two turbulence conditions.

narrowing effect downstream (X/d>5). Additionally, the lateral width of flame in downstream (X/d>15) is slightly higher than the smooth flow condition. This may occur as a result of lateral turbulence effect (I_W) of crossflow. The flame colour for both cases appears similar.

Fig. 4.11 depicts instantaneous images captured from the top camera at high jet velocity (U_j = 4m/s). The flame exhibits similar phenomena for enhanced turbulence as mentioned for figure 4.10. Additionally, the lateral width of the flame is increased due to enhanced crossflow turbulence.
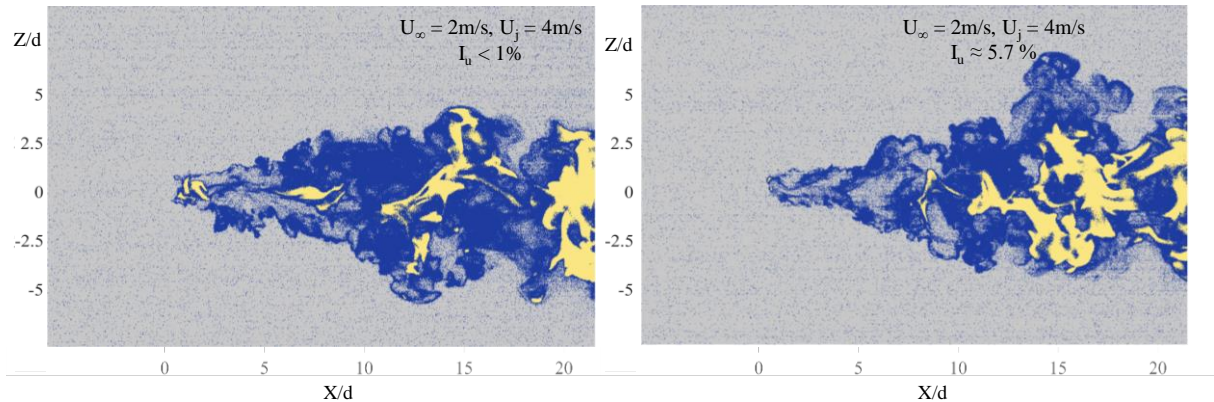
Figure 4.11: Analysis of instantaneous images at U_∞ = 2m/s and U_j = 4m/s for two turbulence conditions (images captured from top camera).

Fig. 4.12a provides a depiction of a segmented image for a side camera (cam 1). Two turbulence conditions (I_u< 1% and $I_u \approx$ 5.7%) are placed side by side for comparison. From the instantaneous images, it is clear that the recirculation zone for enhanced crossflow turbulence is higher than smooth flow. This is discussed in detail in section 4.1. In addition, the colour of the shear layer appears more extended at U_∞ = 4m/s in fig. 4.12a. However, the results are not consistent at U_∞ = 6m/s (fig. 4.12b). Gollahalli et al.(1975) mentioned blue flame as an indication of mixing of air to fuel. As a result, it's hard to assume enhanced crossflow turbulence is beneficial for the air to fuel mixture.
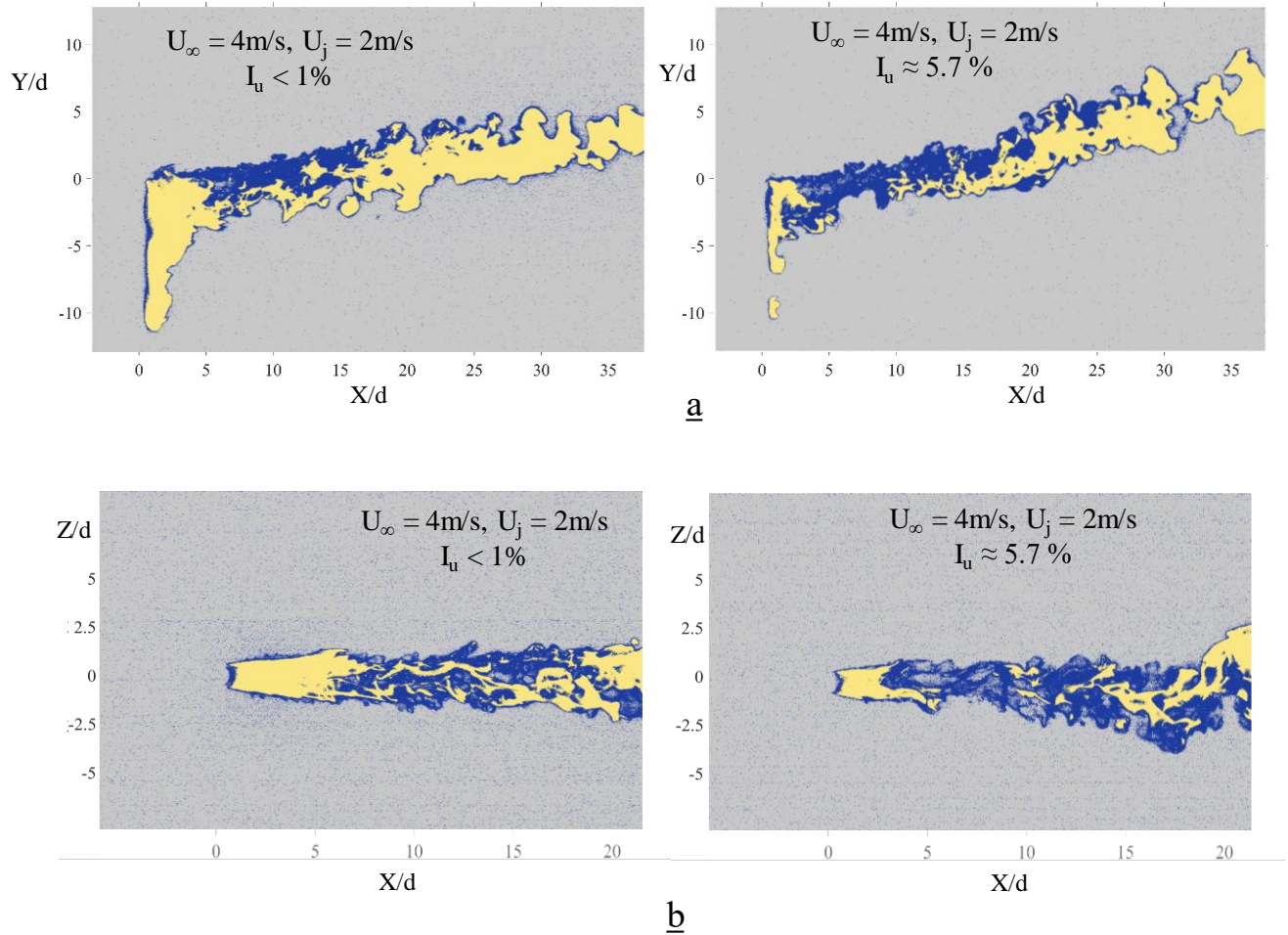
Figure 4.12: Analysis of instantaneous images at U_j = 2m/s for two turbulence conditions when (a) U_∞ = 4m/s, (b) U_∞ = 6m/s (images captured from camera 1).

Fig. 4.13a presents orange to blue flame ratio at different crossflow velocity when the jet velocity is 2m/s. The ratio is obtained from segmented image pixel information. It is observed from the figure that there is no consistent variation of orange to blue flame for different turbulence conditions. At U_∞ = 8m/s, the difference of colour ratio for two turbulence conditions is higher. This is because of the strong recirculation zone for smooth flow condition (where, soot radiating orange flame appears on recirculation zone). When the jet velocity is 4m/s (fig. 4.13b), the ratio of orange to blue flame is higher in smooth flow case. This phenomena indirectly suggests that for a strong jet velocity, enhanced

crossflow turbulence does a better job for air-to-fuel mixing in the near field. However, there is no overall trend to conclude that enhanced crossflow turbulence is beneficial for the air-to-fuel mixture.
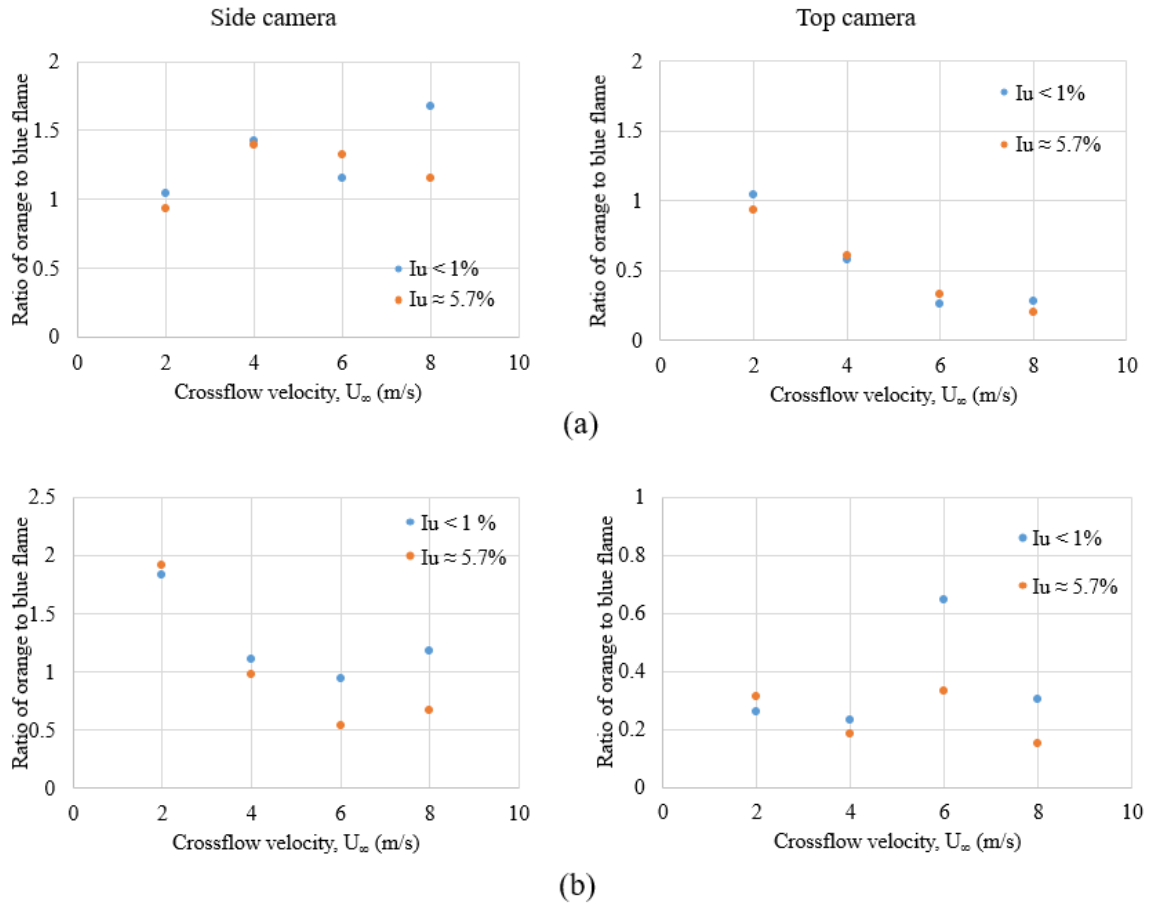
Figure 4.13: Average ratios of orange to blue flames from segmented images at different crossflow velocities for jet velocities (U_j) of (a) 2 m/s and (b) 4 m/s.

4.5 Summary

The effect of turbulence crossflow on jet flame has been analyzed by instantaneous and mean flame images. Full flame is captured using 3 cameras from the side, top camera captures the flame up to 20 diameters (d ≈ 1inch) downstream. Recirculation zone shape, flame dispersion on the vertical and lateral direction are explained based on the mean flame image produced from instantaneous sequential images. Instantaneous images are used to describe discrete flame packet analysis and image segmentation for the different colour channels. Image processing methodologies are explained in appendix A. The brief observation of flame response due to turbulence crossflow is discussed as follows:

- There is a strong recirculation zone formed on the leeward side of the stack in crossflow-dominated flame. For enhanced crossflow turbulence ($I_u \approx 3.7$ %, 5.7%), recirculation zone is smaller comparing to smooth flow ($I_u < 1\%$). This is indirectly a clear indication of comparatively higher pressure on the leeward sidewall for enhanced turbulent crossflow.

- Vertical dispersion or spread of the flame is slightly higher for enhanced crossflow turbulence. However, the spread is not quite significant to mark for all velocity ratios.

- Compared to vertical spread for enhanced turbulence crossflow, flame spreads more on lateral direction due to induced turbulence. Lateral dispersion is significant for crossflow-dominated flame. However, for a strong jet momentum ratio, lateral dispersion is not remarkably varied for turbulent crossflow.

- There is no consistent variation of discrete flame packets for turbulent crossflow.

- Instantaneous flame analysis from segmented image suggests the lateral width of the flame is higher in the near field for smooth flow. There is no consistent variation of shear layer blue flame region for the enhanced turbulent condition.

Chapter 5

5   Conclusion and recommendations

5.1   Conclusion

A previous study from Johnson and Kostiuk (2002) suggested flaring efficiency (or carbon conversion efficiency) reduces in turbulent cross-winds. Johnson et al.(2001) identified that the probable fuel stripping zone is located in the lower portion (near recirculation zone) of crossflow-dominated flames. From their work, it is also evident that unburned fuel exists in between the discrete flame packets (Johnson and Kostiuk, 2002). The main focus of this study is to observe the difference in the visible flame appearance in turbulent cross-winds in order to connect to the previous findings. Turbulent crossflows are generated using passive grids. An empirical equation for methane flame length is provided. Trajectory scaling for flame has been checked at different velocity ratios ($4 \geq r \geq 2$). Visual flame dispersion in the vertical and the lateral directions has been checked for different crossflow conditions.

Carbon conversion inefficiency is higher in the presence of increased crossflow velocity (fig. 1.7). In the presence of strong crossflow, flames appear as crossflow-dominated, which is the regime of interest. In the current study both crossflow-dominated flames and jet-dominated flames are analyzed for different turbulent conditions. Based on the observations in chapter 3 and chapter 4, the following conclusions can be made:

- Flame length can be estimated with good agreement from empirical equations for different flow rates and stack different diameters. The empirical equation will give an estimation of the flame length of natural gas for the site engineers (eqn. 3.3 & eqn. 3.4). The empirical relation is less predictable from the experimental results when a larger recirculation zone appears (fig. 3.8).

- The flame lengths are reduced by 8-10% as an effect of turbulent cross-wind (fig. 3.10). The reduction in flame lengths due to enhanced turbulent cross-wind are observed for both crossflow-dominated and jet-dominated flames. However, when strong downwash flame (larger recirculation zone) appear (fig. 3.11), the flame length for smooth crossflow is smaller than turbulent crossflow.

- The flame recirculation zone behind the stack (on the leeward side) is reduced as a result of strong turbulent cross-winds (fig. 4.1, fig. 4.2, and fig. 4.3). These results occur consistently for crossflow-dominated flames at different velocity ratios.

- From the mean flame images, it is observed that lateral (Z-direction) spread of flames for turbulent cross-winds are higher compare to smooth cross-winds (fig. 4.6 and fig. 4.7). This trend is consistent both for crossflow-dominated flames and jet-dominated flames. The flame spread is greater in the vertical direction (Y-direction) due to enhanced crossflow turbulence (fig. 4.4 and fig. 4.5) for both crossflow-dominated flames and jet-dominated flames.

- Johnson and Kostiuk(2002) observed unburned fuel in between the discrete flame packets using Mie scattering technique. It can be assumed that increased numbers of packets is an indirect indication of reduced carbon conversion efficiency. In this study, it is observed that the discrete flame packets do not change significantly for different turbulent cross-wind conditions (fig. 4.9). This observation is consistent both for crossflow-dominated flame and jet-dominated flames.

- Mean flame colour ratio (orange to blue) suggests a lack of consistent variation of the observed flame colour in the near field for different turbulence conditions. The colour of the flames indirectly indicates a better mixing and less soot formation in fig. 4.13b at U_j = 4m/s for enhanced turbulence (Iu ≈ 5.7%). However, there is no remarkable variation in the ratio of flame colour in fig. 4.13a at U_j = 2m/s for I_u ≈ 5.7%.

Overall, both the flame length and the downwash region decrease as an effect of enhanced turbulent cross-wind (fig. 4.3) for crossflow-dominated flame. Although the fuel flow rate is the same, it is reasonable to consider the two following possibilities:

I. The flaring gas burns within the smaller area to enhance cross-wind turbulence. It may be assumed that for enhanced cross-wind turbulence, good mixing happens in the near field. As a result, the fuel may burn more quickly in the far field. However, there is no consistent evidence from the instantaneous flame images that enhanced turbulence enhances mixing.

II.   In this study, instantaneous images captured the visible flame. It is assumed that there is unburned fuel that exists in between the blue colour mixing layer in the near field, which burns downstream. It is a possibility that a part of the unburnt fuel is stripped out before participating in the burning process. This effect cannot be verified in this study because we only captured the visible flame. Further work is needed to resolve the issue.

5.2   Recommendations

In order to resolve the mechanisms associated with reduced carbon conversion efficiencies in a turbulent crossflow, it is strongly suggested to track the unburned fuel path in the near field for both smooth and turbulent flow conditions. Mie scattering or Schlieren imaging are suggested to conduct to check if there is any fuel stripping happening for enhanced cross-wind turbulence. In this study, the mixing phenomena are explained indirectly by changing the flame colour. An experiment with PIV(particle image velocimetry) would be beneficial to describe the mixing phenomena.

References

Andreopoulos, J. (1989). Wind tunnel experiments on cooling tower plumes: part 1—in uniform crossflow. *Journal of heat transfer*, *111*(4), 941-948.

Vickery, B. J. (1965). On the flow behind a coarse grid and its use a model of atmospheric turbulence in studies related to wind loads on buildings. *NPL Aero Report 1143*.

Baines, W. D., & Peterson, E. G. (1951). An investigation of flow through screens. *Trans. Am. Soc. Mech. Engrs.*, *73*.

Blanchard, J. N., Brunet, Y., & Merlen, A. (1999). Influence of a counter rotating vortex pair on the stability of a jet in a cross flow: an experimental study by flow visualizations. *Experiments in fluids*, *26*(1-2), 63-74.

Bourguignon, E., Johnson, M. R., & Kostiuk, L. W. (1999). The use of a closed-loop wind tunnel for measuring the combustion efficiency of flames in a cross flow. *Combustion and Flame*, *119*(3), 319-334.

Camussi, R., Guj, G., & Stella, A. (2002, 3 10). Experimental study of a jet in a crossflow at very low Reynolds number. *Journal of Fluid Mechanics, 454*, 113-144.

Cifuentes, L., Dopazo, C., Martin, J., & Jimenez, C. (2014, 6 25). Local flow topologies and scalar structures in a turbulent premixed flame. *Physics of Fluids, 26*(6).

Conrad, B. M., & Johnson, M. R. (2019). Mass absorption cross-section of flare-generated black carbon: Variability, predictive model, and implications. *Carbon*, *149*, 760-771.

Cook, N. J. (1978). Wind-tunnel simulation of the adiabatic atmospheric boundary layer by roughness, barrier and mixing-device methods. *Journal of Wind Engineering and Industrial Aerodynamics*, *3*(2-3), 157-176.

Davitian, J., Hendrickson, C., Getsinger, Closkey, R., & Karagozian, A. (2010, 9). Strategic control of transverse jet shear layer instabilities. *AIAA Journal, 48*(9), 2145-2156.

Davidson, L (2014), 'Fluid mechanics, turbulent flow and turbulence modeling', Lecture Notes, Chalmers Institute of Technology, Gothenburg, Downloaded from: http://www.tfd.chalmers.se/~lada/postscript_files/solids-and-fluids_turbulentflow_turbulence-modelling.pdf on July 15, 2019

Elvidge, C., Zhizhin, M., Baugh, K., Hsu, F., & Ghosh, T. (2016). Methods for global survey of natural gas flaring from visible infrared imaging radiometer suite data. *Energies, 9*(1).

Fric, T. F., & Roshko, A. (1994). Vortical structure in the wake of a transverse jet. *Journal of Fluid Mechanics*, *279*, 1-47.

Smith, S. H., & Mungal, M. G. (1998). Mixing, structure and scaling of the jet in crossflow. *Journal of fluid mechanics*, *357*, 83-122.

Getsinger, D. (2012). *Shear layer instabilities and mixing in variable density transverse jet flows* (Doctoral dissertation, UCLA).

Gollahalli, S. R., & Nanjundappa, B. (1995). Burner wake stabilized gas jet flames in cross-flow. *Combustion science and technology*, *109*(1-6), 327-346.

Gollahalli, S., Brzustowski, T., & Sullivan, M. (1975). Characteristics of a Turbulent Propane Diffusion Flame in a Cross-Wind. *Canadian Chemical Engineering Conference.*

Gopalan, S., Abraham, B., & Katz, J. (2004). The structure of a jet in cross flow at low velocity ratios. *Physics of Fluids, 16*(6), 2067-2087.

Hjertager, B. (2014). *Computational analysis of fluid flow processes-A compendium Wind energy View project Combustion and chemical reaction in turbulent flow View project.* University of Stavanger.

Huang, R., & Chang, J. (1994). Coherent structure in a combusting jet in crossflow. *AIAA Journal, 32*(6), 1120-1125.

Huang, R. F., & Chang, J. M. (1994). The stability and visualized flame and flow structures of a combusting jet in cross flow. *Combustion and Flame*, *98*(3), 267-278.

Huang, R. F., & Wang, S. M. (1999). Characteristic flow modes of wake-stabilized jet flames in a transverse air stream. *Combustion and Flame*, *117*(1-2), 59-77.

Johnson, M. R., & Kostiuk, L. W. (2002). A parametric model for the efficiency of a flare in cross-wind. *Proceedings of the Combustion Institute*, *29*(2), 1943-1950.

Johnson, M. R., & Kostiuk, L. W. (2002). Visualization of the Fuel Stripping Mechanism for Wake-Stabilized Diffusion Flames in a Crossflow. In *IUTAM Symposium on Turbulent Mixing and Combustion* (pp. 295-303). Springer, Dordrecht.

Johnson, M. R., Wilson, D. J., & Kostiuk, L. W. (2001). A fuel stripping mechanism for wake-stabilized jet diffusion flames in crossflow. *Combustion Science and Technology*, *169*(1), 155-174.

Kalghatgi, G. (1983). The visible shape and size of a turbulent hydrocarbon jet diffusion flame in a cross-wind. *Combustion and Flame, 52*(C), 91-106.

Kamotani, Y., & Greber, I. (1972). Experiments on a turbulent jet in a cross flow. *AIAA journal*, *10*(11), 1425-1429.

Karagozian, A. (2010). Transverse jets and their control. *Progress in Energy and Combustion Science, 36(5)*, 531-553. Elsevier Ltd.

Karagozian, A. R. (2014). The jet in crossflow. *Physics of Fluids*, *26*(10), 1-47.

Keffer, J., & Baines, W. D. (1963). The round turbulent jet in a cross-wind. *Journal of Fluid Mechanics*, *15*(4), 481-496.

Kelso, R. M., Lim, T. T., & Perry, A. E. (1996). An experimental study of round jets in cross-flow. *Journal of fluid mechanics*, *306*, 111-144.

Kostiuk, L. W., Mejeski, A. J., Poudenx, P., Johnson, M. R., & Wilson, D. J. (2000). Scaling of wake-stabilized jet diffusion flames in a transverse air stream. *Proceedings of the Combustion Institute*, *28*(1), 553-559.

Laneville, A. (1973). *Effects of turbulence on wind induced vibrations of bluff cylinders* (Doctoral dissertation, University of British Columbia).

Laws, E. M., & Livesey, J. L. (1978). Flow through screens. *Annual review of fluid mechanics*, *10*(1), 247-266.

Li, T., Pareja, J., Fuest, F., Schütte, M., Zhou, Y., Dreizler, A., & Böhm, B. (2018, 1 1). Tomographic imaging of OH laser-induced fluorescence in laminar and turbulent jet flames. *Measurement Science and Technology, 29*(1).

Li, X., Hu, L., & Shang, F. (2018, 12 1). Flame downwash transition and its maximum length with increasing fuel supply of non-premixed jet in cross flow. *Energy, 164*, 298-305.

Lim, T., New, T., & Luo, S. (2001). On the development of large-scale structures of a jet normal to a cross flow. *Physics of Fluids, 13*(3), 770-775.

Majeski, A. J. (2000). *Size and shape of low momentum jet diffusion flames in cross flow* (Master's thesis, University of Alberta).

Majeski, A. J., Wilson, D. J., & Kostiuk∗, L. W. (2004). Predicting the length of low-momentum jet diffusion flames in crossflow. *Combustion science and technology*, *176*(12), 2001-2025.

Megerian, S., Davitian, J., Alves, L., & Karagozian, A. (2007, 12 25). Transverse-jet shear-layer instabilities. Part 1. Experimental studies. *Journal of Fluid Mechanics, 593*, 93-129.

Muniz, L., & Mungal, M. G. (2001). Effects of heat release and buoyancy on flow structure and entrainment in turbulent nonpremixed flames. *Combustion and Flame*, *126*(1-2), 1402-1420.

Muppidi, S., & Mahesh, K. (2005, 5 10). Study of trajectories of jets in crossflow using direct numerical simulations. *Journal of Fluid Mechanics, 530*, 81-100.

Nakamura, Y., & Ohya, Y. (1983). The effects of turbulence on the mean flow past square rods. *J. Fluid Mech*, 331-345.

New, T., Lim, T., & Luo, S. (2006, 6). Effects of jet velocity profiles on a round jet in cross-flow. *Experiments in Fluids, 40*(6), 859-875.

Olivier Eiff, B., & Keffer, J. (1997). On the structures in the near-wake region of an elevated turbulent jet in a crossflow. *J. Fluid Mech*, 161-195.

Perry, A., & Chong, M. (1987). A Description of eddying motions and flow patterns using critical-point concepts. *Ann. Rev. Fluid Mech, 19*, 125-55.

R., B. (2012). *Modelling Industrial Flares Impacts.*Enviroware srl.

Roach, P. E. (1987). The generation of nearly isotropic turbulence by means of grids. *International Journal of Heat and Fluid Flow*, *8*(2), 82-92.

Sarkar, D., & Savory, E. (2019). Design of passive wind-tunnel grids using a prediction model for turbulence intensity. *Proceedings of the joint canadian society for mechanical engineering and CFD society of canada international congress*.

Shang, F., Hu, L., Sun, X., Wang, Q., & Palacios, A. (2017). Flame downwash length evolution of non-premixed gaseous fuel jets in cross-flow: Experiments and a new correlation. *Applied Energy, 198*, 99-107.

Su, L., & Mungal, M. (2004, 8 25). Simultaneous measurements of scalar and velocity field evolution in turbulent crossflowing jets. *Journal of Fluid Mechanics, 513*, 1-45.

Shutterstock, Stack flame image, accessed 21st November 2018, <httpsenvironmentaldefence.ca201805315-reasons-why-ab-methane-regulations-dont-cut-it>

J. Tollefson, "'Flaring' wastes 3.5% of world's natural gas" January 11, 2016. [Online]. Available: https://www.nature.com/news/flaring-wastes-3-5-of-world-s-natural-gas-1.19141#ref-link-1. [Accessed: April 1, 2019].

Vita, G., Hemida, H., Andrianne, T., & Baniotopoulos, C. (2018, 7 1). Generating atmospheric turbulence using passive grids in an expansion test section of a wind tunnel. *Journal of Wind Engineering and Industrial Aerodynamics, 178*, 91-104.

Wang, Q., Hu, L., Zhang, X., Zhang, X., Lu, S., & Ding, H. (2015, 12 1). Turbulent jet diffusion flame length evolution with cross flows in a sub-pressure atmosphere. *Energy Conversion and Management, 106*, 703-708.

White, F. M. (2004). Fluid mechanics, 4th edition, McGraw Hill Publisher.

Appendix A:

A.1 Image analysis technique

This appendix explains the methodology of determining the flame length. The image processing technique is discussed with brief explanations. Distinguished figures are provided with explanations to make it clear to the reader. Images of the flame are collected with colour Basler Ac A 1920 cameras as depicted (fig. 2.1) in chapter 2 images. The sensor is CMOS- Sony IMX- 174.

A LabVIEW code is developed to acquire images(fig A.1). The LabVIEW code is simply explained as the consumer-producer loop structure. Where the images are captured in the
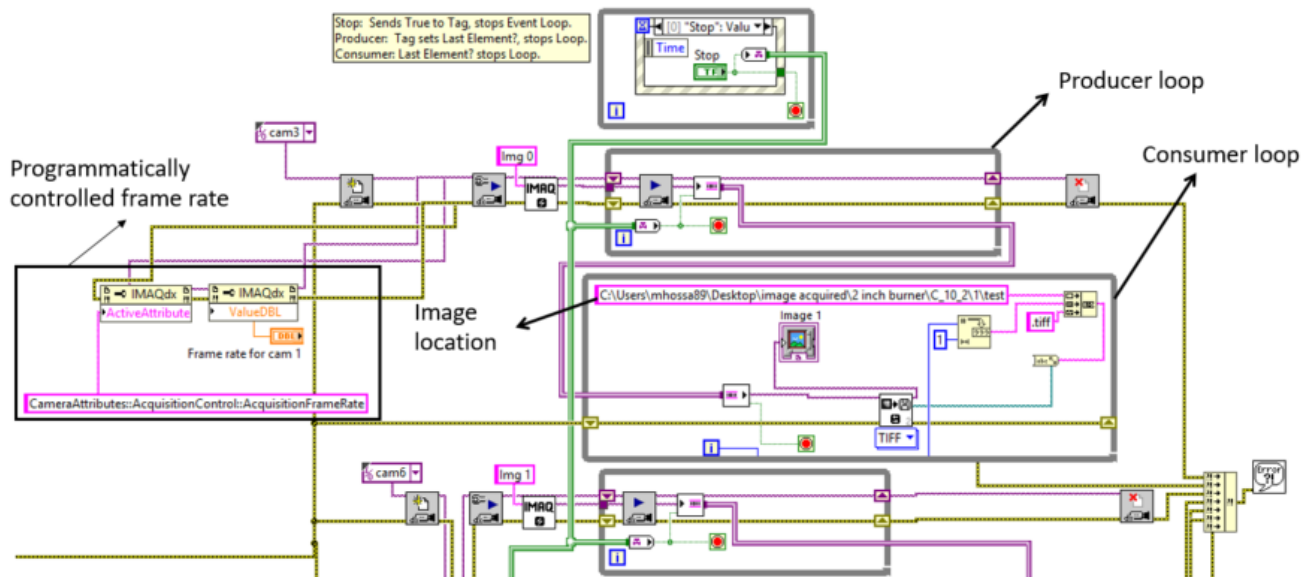

Figure A. 1: Part of image acquisition Labview code(where the symbol represents usual LabVIEW symbol meaning).

consumer loop and send through a wire to producer loop. The consumer loop saves the images in order to the Solid State Disc(SSD) of the laboratory computer. The computer SSD can save the data up to 2.7GB/s which is quite enough to save images without dropping the frame rates significantly.

The frame rate, exposure time, gain and other image acquisition quantities are kept constant during taking the whole sets of experiments for all 4 cameras. 17 mm lens is used to 3 side cameras and 28mm lens is used to top cameras.

With the help of commercial software and LabVIEW, image acquisition is completed. MATLAB is used to analyze the acquired images.

A.2 Segmenting the flame from background

Images of the flame are collected with 3 channel (RGB) colour camera. The output signal of the cameras is saved as 8bit .TIF(Tagged Image Format) file. TIF is an image format file for high-quality graphics without compressing the images like .JPEG file. The resulting .TIF files are simply a list of light intensities, ranging from 0 to 255 for each channel. The single image is then converted to grayscale images which have light intensity 0 to 255 as well. Later, the histogram of a grayscale image is generated(no of pixels vs pixel intensity plot). The derivative of the histogram plot gives an indication to choose cut off pixel value to separate the background from the flame (fig A.2).

The procedure is executed to every 100ms sequential images and keep the flame location record in an array. Later, get the averaged image based on probability of visible flame occurrence on as 100%, 50%, and 10% contour.
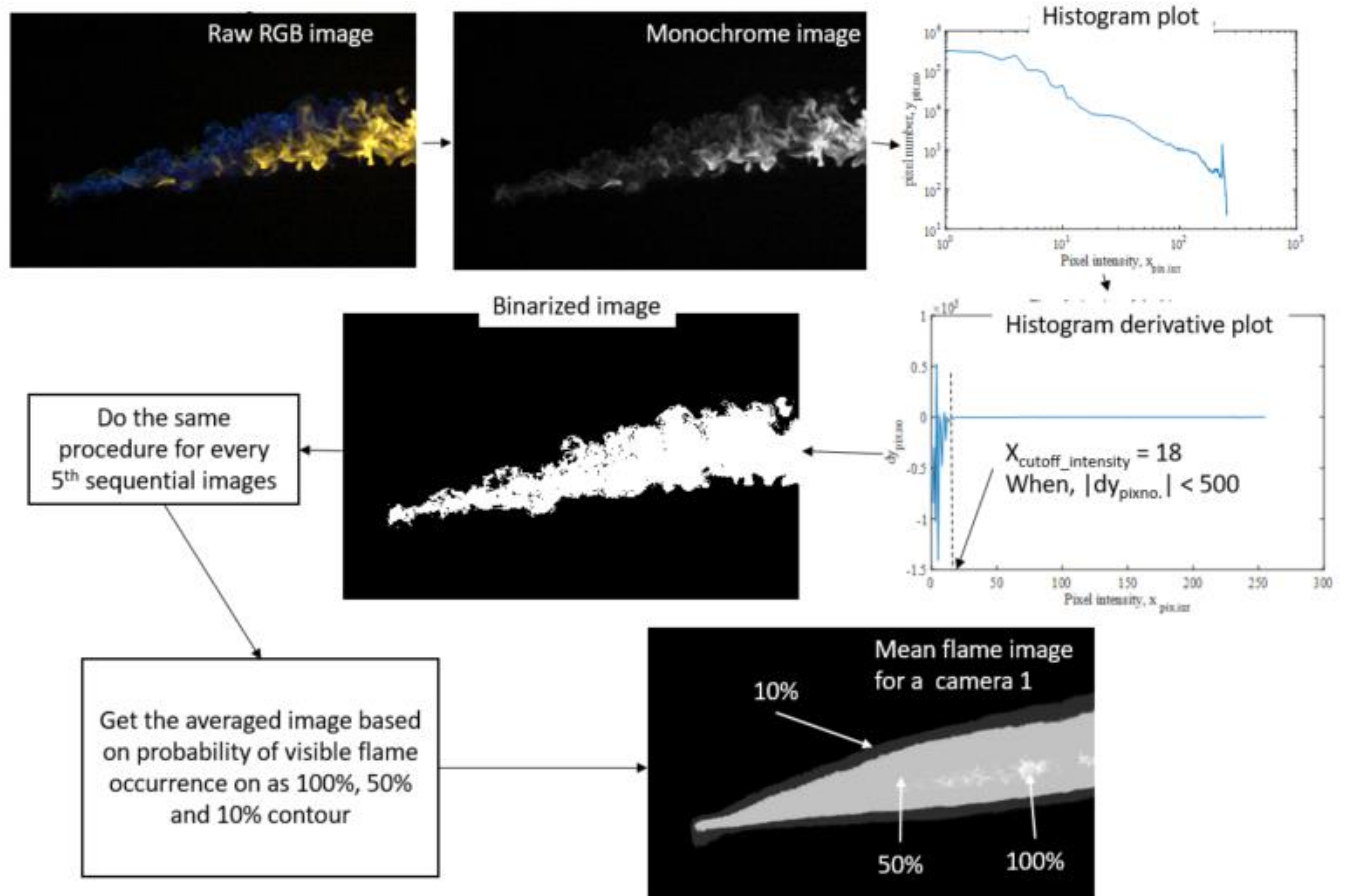
Figure A. 2: Procedure to get mean flame images for individual camera.

A.3   Image the mean flame images

The location of the burner stack for each set of experiments is kept in record. The overlap region in X-direction between camera 1- camera 2 and camera 2-camera 3 is recorded. The relative vertical position(Y-direction) of the side cameras changes their position during the experiments and location is tracked. Based on the record, all three mean images from side cameras are combined to one single image programmatically. Statistically, the combined image represents the mean flame for a particular experimental condition.
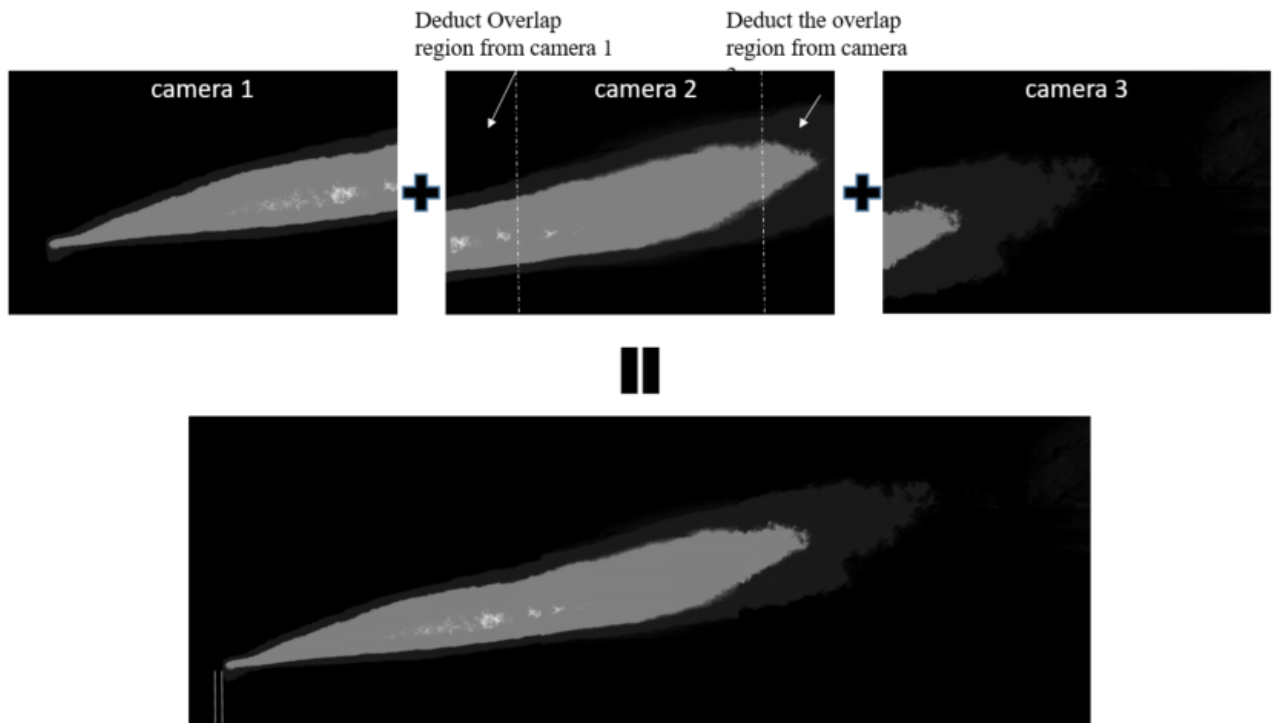

Figure A. 3: Mean image of full flame

A.4 Discrete blob analysis

Instantaneous images from different cameras have been combined to represent a full flame image(fig. A. 4a). The combined images are binarized as an initial step to count discrete flame packets. Image binarization is executed as discussed in section A.1(fig. A. 4b). Discrete flame packets are also defined as a discrete blob in previous analysis. The size and shape of the discrete flame packets are wide in range. In this study, the flame packets are defined from 10 diameter circle sizes to the smallest possible visible flames. The discrete flame packets are labeled with different colours to visualized clearly. This
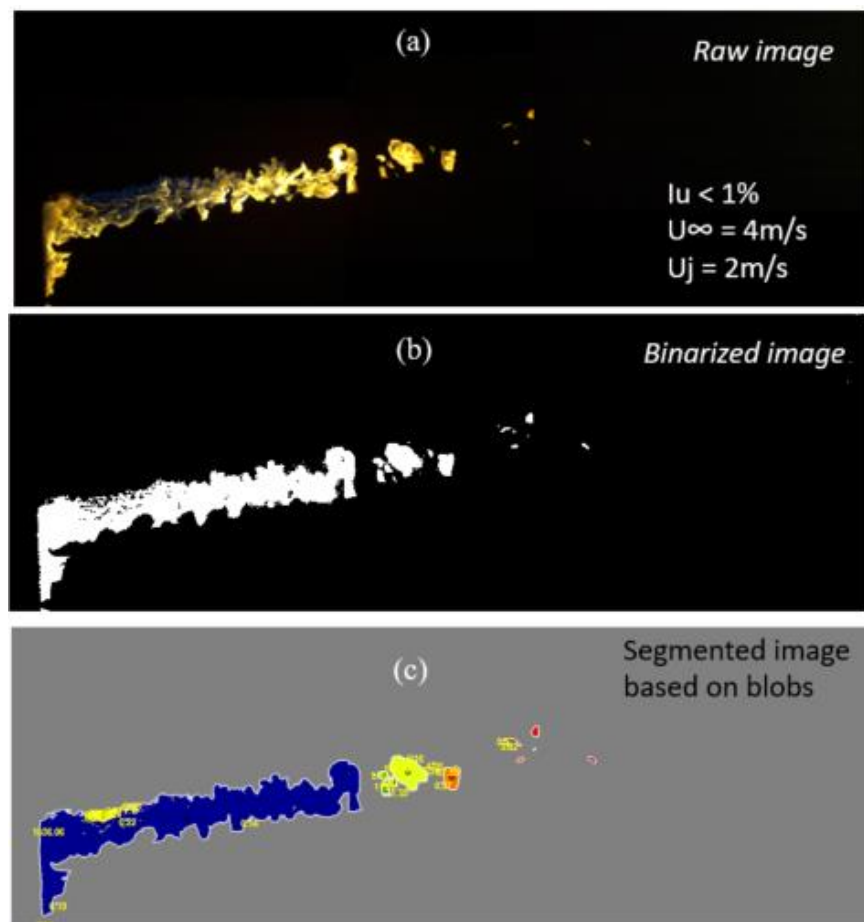

Figure A. 4: Procedure to identify discrete flame packets (U∞ = 4m/s, Uj = 2m/s).

procedure is executed for all the sequential images. The total no. of flame packets are divided by total no. of images to get average flame packets.

The time lag between 1st camera image and 2nd camera image is 4ms (millisecond), 1st to 3rd is 9 ms and 1st to the top camera is 7ms. This is one of the limitations of discrete flame analysis for combined image.

A.5   Colour channel analysis

8bit RGB image has been taken during the experiment. 3 colour channels are present in the individual image. However, segmenting the image based on 3 colour channels may provide a false representation about the true colour of the flame. Fig. A.5 provides a depiction of
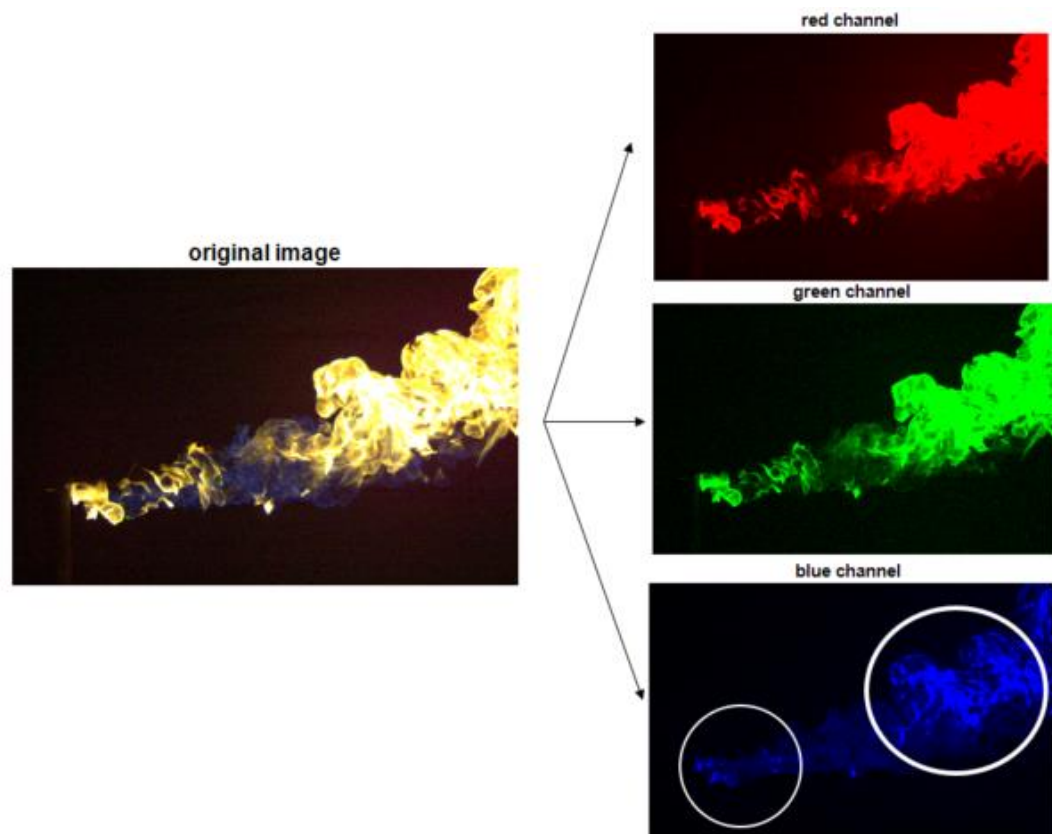

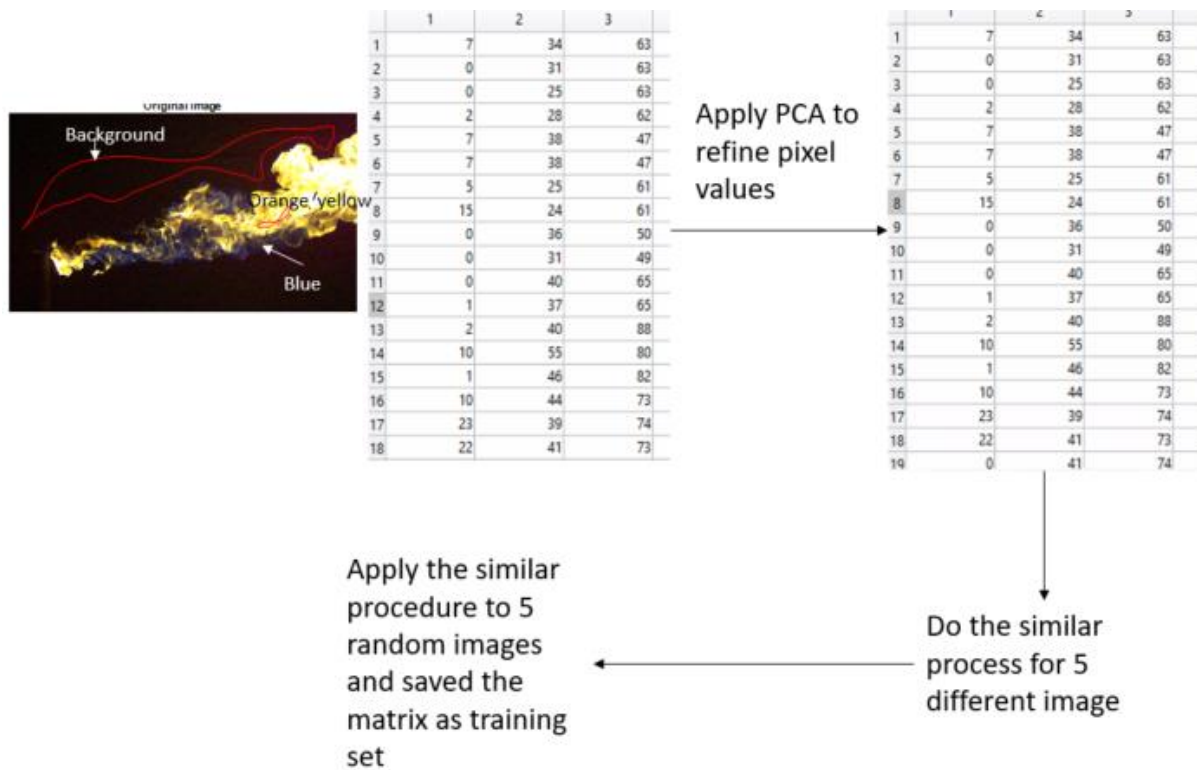**Figure A. 5: Segmenting images based on colour channels.**

Figure A. 6: Steps to prepare training set.

image segmentation to red, green and blue channel. For the current research, it is important to distinguish blue channels in the image. In fig. A.5, the intensity of the blue pixel on far field (marked white circle) is clearly higher than the intensity of the blue field in the near field. However, there is no trace of blue-coloured flame present on the far field. Before segmenting the image based on colours, these issues need to be considered.

To solve this issue, a conventional machine learning algorithm is used to segment the images. The flame image is segmented into 3 classes: background, blue flame, and orangish-yellow flame. 5 images are trained to manually for each turbulent condition for

each camera. Training data for each class are refined using Principal Component Analysis(PCA) method. The training set is tested to check the segmented image and to keep the error less than 5%. The procedure is explained in the following figure.
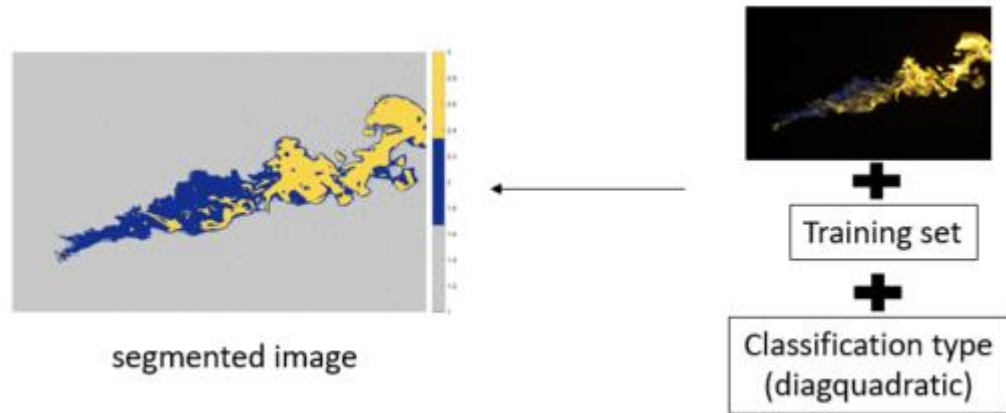

Figure A. 7: Segmenting images from raw RGB image.

Once the training set is formed, entire set images for that particular flow condition can be segmented into three distinct regions: background, blue and orange/yellow flame (fig. A.7). Diagquardratic classifier function is used as classifies with minimal error.

Appendix B.

B.1   Uncertainties in the measurements of crossflow velocity

In order to estimate the uncertainties associated with the velocity measurements, the performance of the cobra probe and pitot tube data are used. Performance of the cobra probe data is compared with pitot tube data taken during the experiments for a wide range of velocities. The data has been taken at the same time. The cobra probe and pitot tube are placed closer and it is made sure that the equipment does not distract each other flow field. Cobra probe readings were sampled at 1250Hz for approximately 60s for 5 different wind tunnel speeds. During the measurements, the cobra probes were set aligned with the flow by visual inspection. From the cobra probe readings and comparing with the pitot tube readings the bias limit, the precision limit and total uncertainties in the velocity measurements by the cobra probe was calculated for each of the 5 discussed test case (table B.1). The number of samples for each of the test cases being larger than 30, in the calculation of precision limits for the cobra probe the value of 't' was considered to be 1.96 (Wheeler and Ganji, 1996).

Pitot tube reading (m/s)	Cobra probe reading (m/s)	standard deviation of cobra probe data, S	Uncertainity of each sample, $w_v = (B^2 + (tS)^2)^{0.5}$	Uncertainity of mean sample, $wv(mean) = (B^2 + (tS/(n)^{0.5})^2)^{0.5}$	Error(%)
2.303	2.2	0.06	0.15	0.10	4.68
4.09	4.11	0.07	0.15	0.02	0.49
6.175	6.12	0.08	0.17	0.06	0.90
8.27	8.07	0.11	0.29	0.20	2.48
10.53	10.07	0.13	0.52	0.46	4.57

Total error is the summation of bias error(B) and precision error(P). The precision error is random in individual measurements and depends on sample size. Meanwhile, experimental equipment is the source of bias error. Bias error is constant under similar similar flow conditions. It can't be eliminated but it can be estimated (Wheeler and Ganji, 1996). For the current crossflow velocity uncertainty, the precision error is less than 0.5% and the maximum overall error is lower than 5%.

B.2   Uncertainties in the measurements of mean image analysis

To get the mean flame image acquisition uncertainty 6 sets of images are considered. Each time approximately 500 images are captured to get a mean flame image for each set. 5 sets of images are captured during August '19 and the sixth set is captured during September '19 (fig B.1). The total area of the flame is calculated in terms of pixel number. The uncertainty analysis is carried over for 3 different flow conditions (table B.2). All of the flow condition is for smooth flow (Iu<1%).
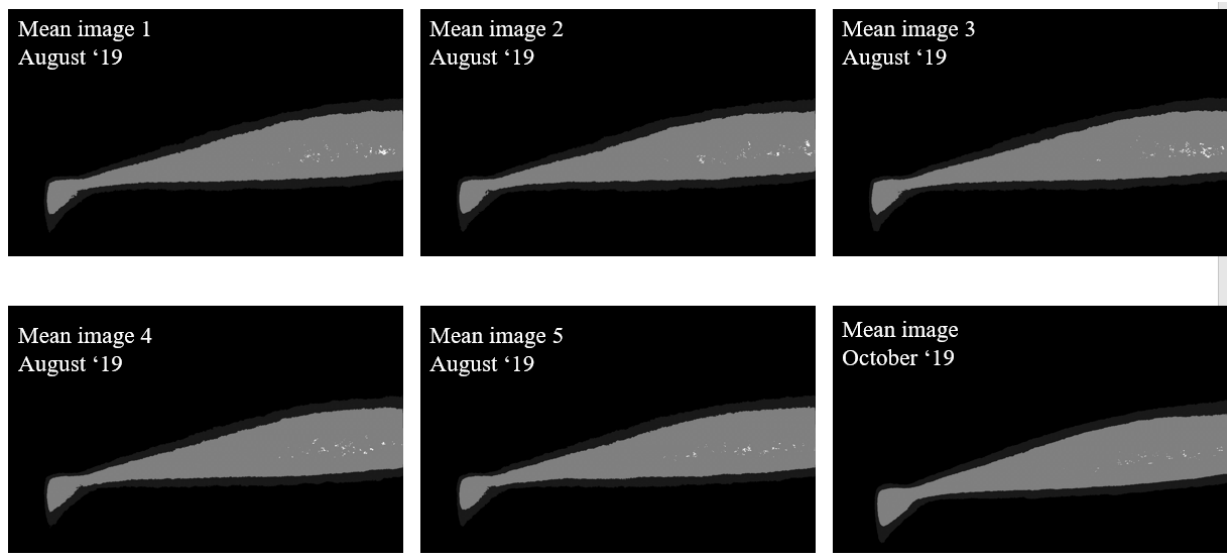

Figure B. 1: Uncertainty analysis for mean flame (U_∞ = 6m/s, U_j = 8m/s).

	Sep '19 acquisition pix reading (no. of pix)	Aug '19 acquisition pix reading (no. of pix, mean value)	standard deviation of Aug '19 acquisition data, S	Uncertainity of each sample, $wv = (B^2 + (tS)^2)^{0.5}$	Uncertainity of mean sample, $wv = (B^2 + (tS/(n)^{0.5})^2)^{0.5}$	Error(%)
$U_\infty = 8m/s$ $U_j = 6m/s$	546886	535120	317	11798.86	18788.27	3.51
$U_\infty = 6m/s$ $U_j = 8m/s$	503574	494080	1298	10154.77	15781.87	3.19
$U_\infty = 10m/s$ $U_j = 6m/s$	571620	570159	353	1759.20	2627.60	0.46

Table B.2 represents error analysis for mean flame images at 3 different velocity pair. It is seen that the maximum error is 3.51%. This error includes bias error(experiments between August '19 and September '19) and precision error. Precision error is less than 0.5%.

Curriculum Vitae

Name	Md Mahbub Hossain
Post-secondary Education and Degrees	Bangladesh University of Engineering and Technology Dhaka, Bangladesh 2011-2016, BSc University of Western Ontario London, Ontario, Canada 2017-2019, MESc
Honours and Awards	Bangladesh Technical Scholarship, 2011-2016 Western Graduate Research Scholarship, 2017-2019
Related Work Experience	Research Assistant University of Western Ontario 2017-2019 Teaching Assistant University of Western Ontario 2018-2019
Publications:	Hossain, M. M., Corbin, D., Kopp, G., 2019 Flow topologies of reactive jet in turbulent cross flow at low velocity ratios. *Proceedings of Combustion Institute – Canadian Section*, Kelowna, British Columbia, Canada Mollik, T., Hossain, M. M., Hasan, S., Sarkar, M. A. R., Zulqarnain, M. A. 2015 Conceptual Study and Analysis of Neutron Diffusion and Moderation in Nuclear Reactor. *International Conference on Mechanical, Industrial and Materials Engineering*, Bangladesh